Relative paleointensity (RPI) and age control in Quaternary sediment drifts off the Antarctic Peninsula

J.E.T. Channell[1*], C. Xuan[2], D.A. Hodell[3], S. J. Crowhurst[3], and R.D. Larter[4]

[1]Department of Geological Sciences, University of Florida, 241 Williamson Hall, POB 112120, Gainesville, FL 32611, USA
[2]School of Ocean and Earth Science, National Oceanography Centre Southampton, University of Southampton, Waterfront Campus, European Way, Southampton SO14 3ZH, UK
[3]Godwin Laboratory for Palaeoclimate Research, Department of Earth Sciences, University of Cambridge, Downing Street, Cambridge, CB2 3EQ, UK
[4]British Antarctic Survey, Madingley Road, Cambridge CB3 0ET, UK.

* corresponding author: jetc@ufl.edu

Abstract

Lack of foraminiferal carbonate in marine sediments deposited at high latitudes results in traditional oxygen isotope stratigraphy not playing a central role in Quaternary age control for a large portion of the globe. This limitation has affected the interpretation of Quaternary sediment drifts off the Antarctic Peninsula in a region critical for documenting past instability of the West Antarctic Ice Sheet (WAIS) and Antarctic Peninsula Ice Sheet (APIS). Here we use piston cores recovered from these sediment drifts in 2015 during cruise JR298 of the RRS *James Clark Ross* to test the usefulness for age control of relative paleointensity (RPI) data augmented by scant $\delta^{18}O$ data. Thermomagnetic and magnetic hysteresis data, as well as isothermal remanent magnetization (IRM) acquisition curves, indicate the presence of both magnetite and oxidized magnetite ("maghemite") in the cored sediments. The magnetite is likely detrital. Maghemite is an authigenic mineral, associated with surface oxidation of magnetite grains, which occurs preferentially in the oxic zone of the uppermost sediments, and buried oxic zones deposited during prior interglacial climate stages. Low concentrations of labile organic matter apparently led to arrested pore-water sulfate reduction explaining oxic zone burial and downcore survival of the reactive maghemite coatings. At some sites, maghemitization has a debilitating effect on RPI proxies whereas at other sites maghemite is less evident and RPI proxies can be adequately matched to the RPI reference template. Published RPI data at ODP Site 1101, located on Drift 4, can be adequately correlated to contemporary RPI templates, probably as a result of disappearance (dissolution) of maghemite at sediment depths >~10 m.

Keywords: West Antarctica, late Quaternary, sediments, magnetic properties, relative paleointensity, oxygen isotopes

1. Introduction

Seven piston cores were collected in 2015 during cruise JR298 of the RRS *James Clark Ross* with lengths in the 9.40-12.93 m range (Table 1). The coring sites are located on a series of sediment drifts off the Antarctic Peninsula (Drifts 4-7) and in the Bellingshausen Sea (Fig. 1). The crests of the sediment drifts at water depths <3000 m were targeted (Table 1) in order to enhance the likelihood of preservation of foraminiferal calcite. The Calcite Compensation Depth (CCD) west of the Antarctic Peninsula has been estimated as lying between 2800 m and 2100 m water depth (Hillenbrand et al., 2003), although the upper Pliocene to Quaternary sediments recovered from Ocean Drilling Program (ODP) Site 1101 (water depth: 3300 m) contain planktic foraminiferal tests in most glacial and interglacial intervals (Barker et al., 2002; Vautravers et al., 2013).

The JR298 piston cores are generally in good condition with minor evidence of coring disturbance often associated with occasional thin sandy layers within a lithology comprising ochre to olive-green to gray mud (clay with fine silt). The muds were derived from turbidity currents that are sourced from glacial sediments on the continental margin and flow along large channels between the drifts. Fine-grained components of the turbidity currents are entrained within a southwestward-flowing bottom current and deposited on the drifts (Rebesco et al. 1996, 2002; Hernández-Molina et al., 2017). Diatom fragments in smear slides of JR298 cored sediments provide ample evidence of sediment reworking. The tops of cores comprise a brownish (ochre) decimeter-scale uppermost oxic layer, with patchy transition to grey and olive-green mud below. The ochre coloration, associated with oxic diagenetic conditions, extends to the base of some of the ~10-12-m long cores.

Sporadic occurrence of the planktic foraminifer *Neogloboquadrina pachyderma* (sin.) has allowed for patchy and discontinuous oxygen isotope data from some of the piston cores. X-ray fluorescence (XRF) core scanning provides ratios such as Ba/Al and Br/Al that can be used as a proxy for marine organic matter (e.g., Ziegler et al., 2008) and surface-water productivity. The a* (red-green) reflectance from spectrophotometry is compared with core photographs, and used to locate surficial and buried oxic zones, together with the Mn/Al ratio where Mn is mobile in sediment pore waters under reducing conditions and forms peaks of Mn-oxide where oxygen is available (Mangini et al., 1990, 2001). Rock magnetic data, principally magnetic hysteresis data, susceptibility versus temperature (κ-T) data, and isothermal remanence (IRM) acquisition curves are used to infer the presence of magnetite and oxidized magnetite ("maghemite") in the sediments. The presence of maghemite affects the coercivity of the natural remanent magnetization (NRM) and the fidelity of the relative paleointensity (RPI) proxies. The objective of this paper is to document the magnetic mineralogy, and assess the potential of RPI as a tool for age control in these sediments.

In Antarctic drifts, RPI has provided age control for a suite of gravity cores (the SEDANO cores) from Drift 7 (Fig. 1) that extend back to ~270 ka (Sagnotti et al., 2001; Macri et al., 2006), and rock magnetic data indicated magnetite as the remanence carrier and general suitability of the sediments for RPI reconstruction (Venuti et al., 2011). ODP Sites 1095 and 1096 (from Drift 7, Fig. 1) from ODP Leg 178 demonstrated the feasibility of obtaining high quality polarity stratigraphies from these sediment drifts (Acton et al., 2002, 2006). One of the ODP Leg 178 sites (Site 1101, Fig. 1) yielded a promising RPI record although the record is affected by core breaks and drilling disturbance in large part because only a single hole was drilled at the site (Guyodo et al., 2001).

2. Sampling, oxygen isotopes, XRF and spectrophotometry

All (7) piston cores collected during cruise JR298 (Table 1) were cut into 1.50-m sections on the core deck, beginning with the base of each piston core. Six of the seven piston cores were split, described, and sampled shipboard during the cruise and the final piston core (Core PC736) was transported in sections to the University of Southampton for processing. U-channel (~$2 \times 2 \times 150$ cm^3) samples were collected from the working halves of each piston core section. Discrete ($2 \times 2 \times 2$ cm^3) samples for further rock magnetic experiments were collected from split sub-cores driven vertically into the top surface of recovered box cores (Table 1). U-channel samples from PC736 were measured at the University of Southampton. All other u-channels were measured at the University of Florida. Rock magnetic data both from discrete samples, and from sub-samples of u-channels, were measured at the University of Florida and at the University of Southampton.

Bulk sediment samples from each piston core were collected shipboard, and then subsequently washed and sieved in order to pick sparse specimens of the planktic foraminifer *Neogloboquadrina pachyderma* from the >150 μm size fraction of the sediment. Where a sufficient number of foraminifera could be obtained at an individual horizon, $\delta^{18}O$ measurements were performed on a Thermo Finnigan MAT253 mass spectrometer fitted with a Kiel IV carbonate device at the Godwin Laboratory for Palaeoclimate Research at the University of Cambridge. Analytical precision for $\delta^{18}O$ on this instrument is estimated to be ±0.08‰.

X-ray fluorescence (XRF) counts for each piston core were measured at the University of Cambridge using an Avaatech XRF core scanner (3rd generation) to obtain semi-quantitative elemental data. The surface of the cores was scraped clean then covered with 4 μm thick SPEXCertiPrep Ultralene foil to avoid contamination and to prevent the cores drying out and cracking. Each section was measured at three different voltages and currents: 10 kV and 750 mA, 30 kV and 500 mA, and at 50 kV and 1000 mA. The entire length of each core was analyzed at 5-mm resolution with an irradiated surface length and width of 5 mm (downcore) and 12 mm (cross core). The count time was 60 s for each measurement. Element intensities were obtained by post-processing of the XRF spectra using the Canberra WinAxil software with standard software settings and spectrum-fit models. The XRF ratios Br/Al, Ba/Al and Ca/Ti were used as proxies for concentrations of organic matter and carbonate, and estimates of surface water productivity. Mn/Al was used to monitor sediment redox state.

We use diffuse-reflectance spectrophotometry to measure a* (red-green) reflectance, and compare a* with core photographs. The primary mineral controlling a* is hematite because a* varies in step with the concentration of hematite estimated from the first derivative of the color spectrum between 555 and 575 nm (Deaton and Balsam, 1991; Debret et al., 2011). Spectrophotometry also provides a measure of the organic content, for comparison with relevant XRF ratios, through determination of the sum of intensities in the "organic" wavelength range (605-695 nm) as defined by Debret et al. (2011).

3. Magnetic Methods

The natural remanent magnetizations (NRM) of u-channel samples collected from the seven piston cores were measured at 1-cm intervals on cryogenic magnetometers designed to measure u-channel samples, at the University of Florida and the University of Southampton, with a 10-cm leader/trailer. Each 1-cm measurement is not independent of adjacent measurements due to the ~4.5-cm width at half-height of the magnetometer response functions (see Weeks et al., 1993; Guyodo et al., 2002; Oda and Xuan, 2014). After initial NRM measurement, stepwise AF demagnetization was carried out with peak field increments of 5 mT in the 10-80 mT peak field range, and then 10 mT steps to 100 mT. Component magnetizations were determined based on NRM data from a uniform 20-80 mT demagnetization interval, for each 1-cm measurement interval, using the standard procedure (Kirschvink, 1980) and the UPmag software (Xuan and Channell, 2009). The maximum angular deviation (MAD) values provide a measure of the definition of each component magnetization direction, with values <5° indicating high quality data. After NRM measurements, the volume magnetic susceptibility (κ) of u-channel samples from six piston cores was measured at 1-cm spacing using a susceptibility track designed for u-channels (Thomas et al., 2003) at the University of Florida. Volume magnetic susceptibility of u-channel samples from PC736 was measured at 1-cm spacing on a susceptibility track at the University of Southampton equipped with a Bartington MS3 meter and 42-mm diameter MS2C sensor loop.

The principal behind relative paleointensity (RPI) estimates using sedimentary records is that variations in magnetizing field strength at the time of NRM acquisition can be determined by normalizing the NRM intensity by the intensity of a laboratory-induced magnetization that activates the same population of grains that carry the NRM, thereby compensating for changes in concentration of NRM-carrying grains down-core (see Banerjee and Mellema, 1974; Levi and Banerjee, 1976; Tauxe, 1993). The normalizer may be anhysteretic remanent magnetization (ARM) or isothermal remanent magnetization (IRM), and the method is applicable if the magnetization is carried by fine-grained (pseudo-single domain or single domain) magnetite or titanomagnetite, with grain sizes $<\sim 10$ μm.

For u-channel samples, ARM was acquired using a 50-μT DC bias field with a 100 mT peak AF, and IRM was acquired in a 0.3 T field and then a 1 T field. The ARM normalizer activates a finer population of magnetite grains than IRM, so the choice of effective normalizer depends on the grain-size distribution of the magnetite. Here, we use ARM acquisition (ARMAQ) and ARM demagnetization to determine slopes of NRM/ARM and NRM/ARMAQ in a chosen demagnetization/acquisition peak AF field range (in this case 20-60 mT), and determine the linear correlation coefficient (r) at 1-cm intervals associated with each of the slopes (see Channell et al., 2002, 2008). Slopes of NRM/IRM were associated with lower r-values, indicating less well-defined slopes, compared to NRM/ARM and NRM/ARMAQ slopes.

Anhysteretic susceptibility (κ_{ARM}) is the ARM intensity divided by the DC bias field used to generate it (in our case 50 μT). The ratio of κ_{ARM}/κ can be used as a proxy for magnetite grain size (King et al., 1983), and uniformity in the ratio is used as indicator of uniformity in magnetite grain size that is one of the important criteria for generating useful RPI data.

After treatment of u-channel samples, cubic (7-cm^3) discrete samples were extracted from several u-channels. The discrete samples were dried in field-free space and wrapped in Al foil. The remanent magnetization was measured before and after wrapping, and then 3-axis IRMs were imposed sequentially and orthogonally for each sample using DC fields of 1.2 T, 0.3 T and 0.1 T (see Lowrie, 1990).

Bulk sediment samples from piston cores and box cores (Table 1) were used to acquire additional rock magnetic data. Hysteresis parameters were acquired using a Princeton Measurements Corporation vibrating sample magnetometer (VSM) at the University of Florida. IRM acquisition curves, using a similar VSM, were acquired at the University of Southampton in order to model coercivity spectra in terms of magnetic components (see Heslop et al., 2002). Susceptibility versus temperature (κ-T) plots, generated using an AGICO Corporation susceptibility meter (KLY-4S with a CS3 furnace) at the University of Southampton, were measured in both argon and air at heating and cooling rates of ~11°C/min.

4. Results

Component magnetization directions, for all cores except one (PC723), determined using NRM data for the 20-80 mT AF peak demagnetization range, yield mean component inclinations around the expected range (77°-79°) for the site latitudes (Fig 2b). Component declinations are poorly determined for steep component inclinations, and are not shown in Fig. 2b. Component inclinations from PC723 are excluded from Fig. 2b because high NRM coercivity throughout the core does not allow complete AF demagnetization at peak fields of 80 mT. A typical orthogonal projection of AF demagnetization data for PC723, from a single measurement position at 739-cm depth, is shown in Fig. 2a. The predominant demagnetization behavior for JR298 samples implies low coercivity for the carrier of NRM (Fig. 2a). On the other hand, discrete intervals of high-coercivity NRM often occur in the uppermost sediments (e.g., at 5-cm depth for PC732, 21-cm depth at PC726, and 10-cm depth for PC736; see Fig. 2a), and in certain discrete intervals at greater depths in some cores (e.g., at 600-cm depth for PC736; see Fig. 2a). MAD values are usually <5°, indicating well defined magnetization components (Fig. 2b). Two cores (PC732 and PC728) show an interval of shallow component inclinations at ~1.4 meters below seafloor (mbsf, Fig. 2b) that will be discussed below.

Hysteresis ratios can be used to delineate single domain (SD), pseudo-single domain (PSD) and multidomain (MD) magnetite grain-sixe mixtures, and assign “mean” magnetite grain sizes through empirical and theoretical calibrations of the Day plot (Fig. 3; Day et al., 1977). The hysteresis data from JR298 cores lie close to the theoretical magnetite grain-size mixing line (Carter-Stiglitz et al., 2001; Dunlop and Carter-Stiglitz, 2006) and, by comparison with empirical hysteresis ratios from sized (unannealed) magnetite (Dunlop, 2002), magnetite grain sizes lie in the 1-20 μm grain size range (Fig. 3). The hysteresis ratios are consistent with the presence of magnetite.

Thermal demagnetization of the 3-axis IRM usually implies low coercivity magnetizations and maximum blocking temperature (~580°C) consistent with the presence of magnetite (Fig. 4a). On the other hand, certain samples indicate a higher coercivity magnetization with ~300°C maximum blocking temperature, often associated with an ochre coloration of the sediments (Fig. 4b,c). Although the magnetic remanence of iron sulfides may unblock at these temperatures, the overall oxic diagenetic conditions favor the presence of maghemite that can invert (at >~250°C) to weakly magnetic hematite or to magnetite.

Susceptibility versus temperature (κ-T) experiments conducted in an argon atmosphere for samples from both piston cores and giant box cores (Table 1) show an abrupt decrease in susceptibility at ~580°C (Fig. 5), indicating the presence of magnetite that is assumed to be largely detrital in origin but with an important contribution from thermal alteration during the heating experiment indicated by the increase in susceptibility of the cooling curves relative to the heating curves. The difference between the heating and cooling curves is most apparent for samples that feature an asymmetric "hump" in the heating curve where the susceptibility decrease associated with the "hump" occurs in the 280-330°C temperature range (Fig. 5). The "hump" is not present in the cooling curves and we associate this "hump" with the presence of oxidized magnetite (maghemite) that reverts to magnetite and hematite on heating above 300°C in an argon atmosphere. Inversion temperatures of maghemite (to hematite in air or magnetite in an inert atmosphere) have been reported in the 250-900°C range dependent on crystallinity, impurities, particle morphology, and grain size with grain sizes <5 μm having low inversion temperatures (de Boer and Dekkers, 1996; Gendler et al., 2005).

Comparison of a* reflectance values with the core photographs indicates that higher values of a* reflectance, as expected, correspond with reddening of sediment color (Fig. 6). The depths corresponding to κ-T curves (Fig. 5) are marked by red arrows in Figure 6, and arrows with asterisks indicate the presence of the "hump" in the κ-T curves (Fig. 5) that correspond with reddened intervals in core images and high values of a* (Fig. 6). Reddened intervals and high values of a* correspond to increased values of the median destructive field (MDF) of NRM that we associated with the maghemitization process (Fig. 6). There is no evidence for the presence of hematite in thermomagnetic remanence data (Fig. 4), possibly implying fine (superparamagnetic) grain sizes for pigmentary hematite. A hematite "tail" is apparent in κ-T data above 600°C (Figs. 5 and 7). As the susceptibility of hematite is ~3 orders of magnitude lower than those of magnetite and maghemite, susceptibility values associated with hematite are masked by the presence of magnetite and maghemite.

All experiments in Figure 5 were conducted in an argon atmosphere. Susceptibility versus temperature (κ-T) experiments for some samples were carried out in Ar and in air (Fig. 7). The heating curves (Fig. 7) are often similar for the two atmospheres although for samples from PC734 and PC727 heating in Ar apparently produced more magnetite (with its ~580°C susceptibility unblocking) than for the same sample heated in air. Heating in air also produced a more distributed decrease of susceptibility above 600°C, implying more oxidized heating products. Both heating and cooling in air yielded more distinctive susceptibility unblocking the vicinity of 700°C. For the cooling curves (Fig. 7b), the experiments in Ar generate higher susceptibility, implying enhanced concentrations of magnetite in the alteration products, while the experiment in air often led to lower susceptibility presumably due to alteration of maghemite mostly to hematite (rather than magnetite). It appears that magnetite is the dominant thermal alteration product after seafloor maghemitization of sedimentary magnetite. Coarse-grained maghemite in plutonic rocks is often identified by its inversion to hematite at high temperatures (Özdemir and Banerjee, 1984; Gehring et al., 2009) that is manifest by reduced susceptibility on cooling, and this κ-T behavior has been seen in proximal sediments from the Antarctic Peninsula where maghemite-rich grains are interpreted as derived from neighboring intrusive rocks exposed on land (Reilly et al., 2016).

The gradients (first derivatives) of IRM acquisition curves of samples from varying core depths are shown in Fig. 8. Many samples show asymmetry in the gradient of the IRM acquisition curves on a logarithmic field scale, indicating likely mixing of multiple coercivity/mineral phases (see Heslop et al., 2002). In the case of PC736, the higher coercivity IRM gradients at sediment depths of 0.1 m, 0.15 m and 6 m (Fig. 8) correspond to intervals of elevated a* where "humps" in κ-T heating curves are observed (asterisks in Fig. 6). For PC726 (GBC725), it is the uppermost part of the core (above 0.44 m depth) and the sample at 6 m that display higher coercivity IRM gradients (Fig. 8), again corresponding to high a* values and ochre sediment color (Fig. 6). For PC723, only the lowermost sample at 11.09 m shows a lower-coercivity IRM gradient (Fig. 8), consistent with the presence of "humps" in κ-T curves in all samples from this core other than the 11.09-m sample (Fig. 5). For PC727, the higher coercivity IRM gradients predominate (Fig. 8), consistent with the prevalence of "humps" in κ-T curves (Fig. 5).

IRM acquisition gradient curves can be modeled in terms of coercivity populations using the method of Heslop et al. (2002). As examples for PC732 and PC736, we modeled two samples from 4 m depth (PC736) and 6.4 m depth (PC732) (Fig. 8, right column) where the gradient curves are more symmetric (Fig. 8, left column) and can be modeled fairly well by a single low coercivity component associated with magnetite. For all other cores shown in Fig. 8, the more asymmetric IRM gradient curves can be modeled by two coercivity components, one centered at ~60 mT and the other at 117-146 mT (Fig. 8). We associate the higher coercivity component with maghemitization of magnetite and the lower coercivity component with unaltered magnetite.

For PC736, PC732, PC728 and PC726, we show the slopes of NRM/ARM and NRM/ARMAQ determined in the 20-60 mT demagnetization/acquisition range, with linear correlation coefficients (r) where values close to unity (>0.9) indicate well defined slopes (Fig. 9). The magnetite grain size proxy (κ_{ARM}/κ) for each core is compared with volume susceptibility, measured on u-channel samples, and a* reflectance. In the lower frames of Fig. 9, we show an attempt to produce an age model that involves the correlation of the NRM/ARM slope (RPI proxy) to a reference RPI template. For sites that have $\delta^{18}O$ data, the available $\delta^{18}O$ data on the trial age models are compared with the LR04 benthic oxygen isotope template (Lisiecki and Raymo, 2005). Sedimentation rate plots (Fig. 9) indicate the ages associated with tie-points for each age model (Table 2). The calibrated template for RPI was constructed using the PISO stack (Channell et al., 2009) beyond 40 ka, and the overall stack from Channell et al. (2018) for the 0-40 ka interval.

PC736, PC732 and PC728 exhibit low values of a* reflectance (<0) below the surficial oxic zone (Fig. 9). For these three cores, we hypothesize that maghemite in the surficial oxic zone is largely reduced on burial below a few tens of centimeters depth. For PC726, the values of a* in the surficial oxic zone are only slightly elevated, but a* values are also elevated at depth in the 5.0-6.5 mbsf interval (Fig. 9). The sparse oxygen isotope data for PC726 are consistent with an age model in which the available $\delta^{18}O$ values denote the marine isotope stage (MIS) 5/6. The Br/Al XRF ratio for PC726 implies a discrete peak in marine organic matter, associated with the higher abundance of foraminifera, and very rare foraminifera outside this Br/Al peak may be reworked from MIS 6.

Cores PC723, PC727 and PC734 did not yield RPI data that could be adequately matched to the reference template. For PC723, intervals of enhanced a* reflectance correspond to core reddening (Fig. 6), as well as to hematite concentration estimated from the first derivative of the color spectrum between 555 and 575 nm (Fig. 10). Pigmentary hematite is not observed in thermomagnetic remanence properties, and is therefore inferred to be predominantly ultra-fine grained (superparamagnetic) hematite produced together with maghemite in surficial oxic zones. Intervals of high a* reflectance also correspond to relatively higher concentrations of marine organic matter as measured by Br/Al and Ba/Al and increased carbonate content from Ca/Ti ratios (Fig. 10). The spectrophotometric intensity in the "organic" wavelength range (605-695 nm) as defined by Debret et al. (2011) also implies higher organic matter content associated with reddened intervals (Fig. 10). On the other hand, the agreement among the various proxies for organic matter is poor, possibly reflecting the overall low concentrations of organic matter in these sediments (<0.3%), and differences in the sensitivity of the proxies to organic matter. The “organic” wavelength range has been tested for "fresh" chlorophyl in lake sediments (Das et al., 2005) however, in the Antarctic sediment drifts, the chlorophyll has low concentration and may be diagenetically altered.

In 1998, a single hole was drilled at ODP Site 1101 located on Drift 4 (Fig. 1). At this site, Guyodo et al. (2001) isolated a low coercivity magnetization component to identify both the Matuyama-Brunhes boundary at ~55 mbsf, indicating a mean Brunhes sedimentation rate of 7.5 cm/kyr, and the Jaramillo and Olduvai subchronozones. Drilling disturbance and poor core recovery in the Brunhes Chronozone did not allow the Brunhes RPI record to be resolved, however, an RPI record from NRM/ARM was resolved from u-channel samples from the base of the Brunhes Chronozone to the base of the Jaramillo Subchronozone (Guyodo et al., 2001). The RPI record from 700 ka to 1.1 Ma was compared with records from elsewhere available at the time. The extended Site 1101 RPI record back to 1.6 Ma can now be matched to contemporary reference templates not available to Guyodo et al. (2001), and a reasonable match can be achieved to the PISO/NARPI (Channell et al., 2009; 2016) reference template (Fig. 11). The resulting age model, based on the RPI correlation, results in low values of susceptibility at Site 1101 matching low (lighter) values (corresponding to interglacial stages) in the LR04 (Lisiecki and Raymo, 2005) reference $\delta^{18}O$ record (Fig. 11). This susceptibility/$\delta^{18}O$ correlation can be attributed to higher biogenic content (dilution of detrital/terrigenous input) during interglacial stages.

5. Discussion

This work constitutes a test of the potential of RPI proxies for generating age models in Quaternary drift sediments off the Antarctic Peninsula (Fig. 1). This is an important issue in view of the paucity of foraminiferal calcite in the region that limits traditional oxygen isotope stratigraphy, and the critical importance of the drifts for monitoring past instability of the West Antarctic Ice Sheet (WAIS) and Antarctic Peninsula Ice Sheet (APIS).

For cores other than PC723, component inclinations resolved in the 20-80 mT AF demagnetization range have low MAD values, implying adequate definition of component directions, and component inclinations are consistent with the expected inclination for the site latitudes assuming a geocentric axial dipole field (Fig. 2b). Interestingly, low component inclinations are observed in two cores (PC728 and PC732) at ~1.3 mbsf (Fig. 2b). In both cores, this depth corresponds to an age of ~13 ka that coincides with an apparent magnetic excursion observed on the Iberian Margin in Core MD01-2444 (Channell et al., 2013).

Magnetite is a ubiquitous detrital or biogenic phase in marine sediments, and is responsible for the “primary” magnetizations that record magnetic polarity stratigraphy and relative paleointensity (RPI) proxies. Magnetite or titanomagnetite can be identified by blocking temperature and coercivity spectra. Authigenic maghemite or titanomaghemite is ubiquitous in the oxic zone of pelagic sediments, typically the uppermost few decimeters of the sediment sequence, may form as oxidized coatings on magnetite grains, and undergoes dissolution as sediment is buried below the oxic zone (Torii, 1997; Smirnov and Tarduno, 2000; Yamazaki and Solheid, 2011; Kawamura et al., 2012; Channell and Hodell, 2013). Authigenic maghemite and pigmentary hematite formed in the surficial oxic zone often constitute the most reactive iron phase present, and as a result, dissolution of these phases at the oxic/anoxic boundary is often associated with reduction of pore-water sulfate, availability of sulfide ions, and the formation of iron sulfides (e.g., Canfield, 1989). Although the dissolution of maghemite at the oxic/anoxic boundary does not appear to affect RPI proxies, at least in some pelagic sediments (Yamazaki and Solheid, 2011), the progression of maghemitization must eventually compromise RPI proxies.

Natural seafloor maghemitization of magnetite produces a complex mixture of non-stoichiometric magnetite in oxidative solid solution between magnetite and maghemite such that individual phases may be difficult to identify and have variable magnetic properties (Gehring et al., 2009). The process of low-temperature oxidation of titanomagnetite to titanomaghemite probably comes about by diffusion of Fe^{2+} ions from the B (octahedral) sublattices close to grain surfaces (Freer and O'Reilly, 1980; Dunlop and Özdemir, 1997). Such authigenic maghemite is likely to be non-stoichiometric and incorporate dislocations and variations in composition that increase the effective coercivity compared to stoichiometric magnetite (e.g., Petersen and Vali, 1987). Mossbauer spectra and X-ray diffraction (XRD) have proven useful for identifying both magnetite and maghemite (e.g., Yamazaki and Solheid, 2011; Xuan and Channell, 2010; Xuan et al., 2012), although both require magnetic extraction that can cause grain-surface oxidation in magnetite. The absence of the low-temperature Verwey transition can be diagnostic of maghemitization of magnetite (Özdemir et al., 1993; Torii, 1997; Smirnov and Tarduno, 2000), although magnetite grain size and cation substitution also affect the manifestation of the transition (Aragon et al., 1985). Maghemite is metastable on heating and converts to hematite and/or magnetite (in an inert atmosphere) over a wide range of temperatures above ~250°C (De Boer and Dekkers, 1996; Gendler et al., 2005), and this property has been used to identify maghemite formed in the oxic zone close to the sediment-water interface of pelagic sediments (e.g., Xuan and Channell, 2010; Kawamura et al., 2012).

Our investigation of magnetic properties of JR298 sediments implies the presence of (titano)magnetite and maghemite (Figs. 3-5, 7 and 8). The dominance of magnetite is seen in the close correspondence of hysteresis ratios to the magnetite grain-size mixing line (Fig. 3). From other studies of pelagic sediments, maghemite formed in the surficial oxic zone displaces the mixing line away from the origin of the Day plot (Smirnov and Tarduno, 2000; Kawamura et al., 2012; Channell and Hodell, 2013), into a region associated with superparamagnetic grains, however, this displacement is not seen in our study (Fig. 3).

Thermomagnetic experiments show maximum blocking temperatures consistent with the presence of magnetite (Figs. 4 and 5). The presence of maghemite is implied by characteristic "humps" in κ-T heating curves that disappear on cooling (Figs. 5 and 7), and by high coercivity components with low blocking temperature (Fig. 4). The gradients of IRM acquisition curves in some samples can be modeled in terms of two coercivity populations, consistent with the presence of magnetite and maghemite (Fig. 8). Pigmentary hematite is responsible for core reddening and controls a* reflectance (Figs. 6 and 10) but is not manifest in thermomagnetic remanence properties, implying fine (superparamagnetic) hematite grain sizes.

Previous paleomagnetic results from the SEDANO cores from Drift 7 (Fig. 1) have been interpreted in terms of magnetite including a "magnetically hard titanomagnetite" (Venuti et al., 2011), and the RPI records have been thought to represent the geomagnetic field intensity (Sagnotti et al., 2001; Macri et al., 2006). Venuti et al. (2011) observed displacement of hysteresis ratios away from the origin of the Day plot (Fig. 3) into the superparamagnetic region of the plot, interpreted here as indicative of the presence of maghemite, and analagous "humps" in κ-T curves (see Fig. 4 of Venuti et al., 2011) are irreversible on cooling.

At ODP Site 1096 (Fig. 1), a high coercivity magnetic phase above 18 mbsf, denoted by elevated values of coercivity of remanence (H_{cr}), is not present below this depth

(Brachfeld et al., 2001). The H_{cr} values are higher than expected for stoichiometric magnetite, and may indicate maghemite in an expanded surficial oxic zone.

In the Antarctic drifts, low organic carbon content (<0.3 %) and low rates of pore water sulfate reduction in the interval penetrated by the ~10-m long cores, results in arrested down-core maghemite/hematite dissolution relative to “normal” pelagic environments. We do not have pore water sulfate data from JR298 piston cores; however, at ODP Site 1101 (Drift 4, Fig. 1) seawater sulfate values are observed down to ~25 mbsf with progressive decrease in sulfate values below that depth to 125 mbsf (Shipboard Scientific Party, 1999).

In some JR298 cores, such as PC732 and PC736, decimeter-scale surficial oxic zones undergo maghemite/hematite dissolution at depth leading to low values of a* below the surficial zone (Figs. 6 and 9). On the other hand, other cores such as PC726, PC723 and PC727 feature “buried oxic zones” denoted by high values of a* at depth (Fig. 6). The buried oxic zones are associated with higher than background organic carbon (Fig. 10) indicating that arrested sulfate reduction does not explain oxic zone burial, because higher organic carbon content would be expected to enhance microbial sulfate reduction (Froelich et al., 1979; Westrich and Berner, 1984). It appears from the preliminary age model for PC726 that the buried oxic zone at 5.0-6.5 mbsf corresponds to MIS 5 (Fig. 9). Similarly, the trial age model for PC723 (Fig. 10g), albeit of very poor quality based on NRM/ARM ratios for two demagnetization steps and a few $\delta^{18}O$ values, also implies that reddened intervals correspond with interglacial stages, in this case MIS 5 and MIS 7. We therefore associate oxic zones with oxygenated bottom waters during interglacial stages, and not primarily with variable maghemite/hematite dissolution associated with variable pore-water sulfate reduction. Similar glacial-interglacial variations in oxygen concentrations have also been inferred for the Southern Ocean by other studies (Jaccard et al., 2016; Lu et al., 2016) possibly associated off the Antarctic Peninsula by activity and location of oxygenated SW-flowing Weddell Sea Deep Water (Giorgetti et al., 2003; Hillenbrand et al., 2008a). Low concentrations of labile (marine) organic are also found in sediments from the Arctic Ocean (Stein et al., 2003) where an analogous presence of authigenic maghemite in an expanded surface-sediment oxic zone has been documented (Channell and Xuan, 2009; Xuan and Channell, 2010; Xuan et al., 2012).

Inspection of core photographs from ODP Site 1101 (Barker et al., 1999) collected from Drift 4 (Fig. 1) indicates that, at least at this site, the ochre coloration, usually indicative of the oxic zone, disappears at ~12 mbsf, implying that authigenic maghemite is lost at depth. This conclusion is supported by the lack of evidence for high-coercivity remanence carriers in the upper Matuyama Chronozone at ODP Site 1101 (Guyodo et al., 2001), and by the observation that RPI data for this interval can be adequately matched to contemporary RPI reference templates (Fig. 11).

6. Conclusions

Maghemitization of magnetite, with pigmentary hematite, restricts the use of RPI as a chronological tool in JR298 sediments, at least in the sampled depth intervals. Buried oxic zones denoted by reddened sediment and higher a* values appear to be associated with interglacial stages (MIS 1, 5 and 7) and their burial is attributed to oxygenation of bottom water during interglacial stages, combined with low concentrations of labile organic matter that delays the dissolution of pigmentary hematite and maghemite that contribute to sediment reddening. Cores that are less affected by authigenic maghemite growth (Cores PC736, PC732, PC728 and PC726) yield RPI proxies that can be adequately correlated to the RPI reference template (Fig. 9).

In most pelagic environments, the oxic/anoxic boundary is observed at decimeter-scale depths whereas oxic/anoxic boundaries at depths up to ~10 m or more are typical for the Antarctic sediment drifts owing to low concentrations of labile (marine) organic matter. RPI proxies from the Matuyama Chronozone at ODP Site 1101 (Guyodo et al., 2001) located on Drift 4 (Fig. 1) can be matched to calibrated RPI templates (Fig. 11) probably due to the absence of maghemite in this interval at this site.

The association of higher than background organic carbon and biogenic components with interglacial stages has been one of few tools for Quaternary age control in marine sediments from this region (e.g., Hillenbrand et al., 2008b), and this study broadly supports this association. RPI-based age control augmented by scant $\delta^{18}O$ data can be applicable in the west Antarctic sediment drifts, although the RPI proxies are compromised by diagenetic maghemitization of magnetite in the surficial oxic zone and buried oxic zones deposited during interglacial climate stages.

Acknowledgements

We acknowledge the pivotal role of the Captain, officers and crew of RRS *James Clark Ross*. We thank Maricel Williams for picking the foraminifera for the isotopic measurements, Claire Allen for discussion of diatom reworking, and Claus-Dieter Hillenbrand for help with core processing. This study forms part of the British Antarctic Survey Polar Science for Planet Earth Programme. We acknowledge grants from UK NERC (NE/J006513/1 and NE/J006548/1), and from the US NSF (OPP 1542579).

Figure Captions

Fig. 1. Location map for sites occupied during Cruise JR298 (red circles) where piston cores (PC) and giant box cores (GBC) were collected (Table 1). Sediment Drifts 4 to 7, and locations of Ocean Drilling Program (ODP) Sites 1095, 1096, and 1101 (yellow circles) are indicated.

Fig. 2 (a) Orthogonal projections of NRM data from the 0-100 mT AF peak field demagnetization interval showing complete demagnetization of NRM (predominant behavior) with examples of high coercivity natural remanant magnetization (NRM) for piston cores PC732 at 5-cm depth, PC723 at 739-cm depth, and PC736 at 10-cm depth and 600-cm depths. Red (blue) lines/symbols represent projection of vector end-points on the vertical (horizontal) plane. (b) Component inclination and maximum angular deviation (MAD) values for piston cores PC726 (green), PC727 (dark blue), PC728 (light blue), PC732 (black), PC734 (orange) and PC736 (red). Component inclinations were computed for a uniform 20-80 mT peak field demagnetization interval. Note interval of low component inclinations at ~1.4 mbsf (meters below seafloor) for PC728 and PC732.

Fig. 3. Magnetic hysteresis plot with single domain (SD), pseudo-single domain (PSD) and multidomain (MD) fields according to Day et al. (1977). The hysteresis ratios for JR298 samples (red dots on left plot and color-coded on right plot) lie close to the theoretical magnetite grain size mixing line shown by black squares (Carter-Stiglitz et al., 2001; Dunlop and Carter-Stiglitz, 2006) and to empirical hysteresis ratios from sized (unannealed) magnetite (blue triangles, Dunlop, 2002).

Fig. 4. Thermal demagnetization of a 3-axis isothermal remanent magnetization (IRM) imposed sequentially and orthogonally in DC fields of 1.2T, 0.3T and 0.1T (see Lowrie, 1990). The higher coercivity magnetizations with maximum blocking temperatures of ~300°C (4b and 4c) are consistent with authigenic maghemite that disassociates below this temperature. The low-coercivity magnetization with maximum blocking temperature of 580°C is consistent with detrital magnetite.

Fig. 5. Susceptibility versus temperature (κ-T) curves measured in an argon atmosphere. The depths below seafloor (m) are shown for each curve. Heating curves are solid lines, and cooling curves are dashed lines. The “humps” at 200-325°C in the heating

curves are interpreted as evidence for the presence of maghemite that disassociates to magnetite and other products in an inert atmosphere in this temperature range.

Fig. 6. Core photographs compared with a* reflectance data for PC736, PC726, PC723 and PC727 (black curves). The blue curve for PC736 denotes the median destructive field (MDF) of NRM. Red arrows mark locations of samples used to generate κ-T curves (Fig. 5). Asterisks mark samples that display "humps" in the κ-T heating curves (Fig. 5), associated with maghemite, that correspond to higher a* values and reddening in core photographs.

Fig. 7. Susceptibility versus temperature (κ-T) curves for samples measured both in an argon atmosphere (dashed lines) and in air (solid lines) during heating (left) and cooling (right). The core and depth below seafloor (m) are shown for each curve.

Fig. 8. Gradient (derivative) of IRM acquisition curves, plotted on a logarithmic applied field scale, of samples from varying depths from piston cores (PC) and giant box cores (GBC) (left panels), and one- or two-component decomposition of one IRM gradient from each core (right panels).

Fig. 9. Cores PC736, PC732, PC728 and PC726: relative paleointensity (RPI) proxies (NRM/ARM and NRM/ARMAQ) and accompanying linear correlation coefficients (r) with κ_{ARM}/κ (proxy for magnetite grain size), and volume susceptibility, plotted against meters below seafloor (mbsf). Lower frames show match of RPI proxy (blue, NRM/ARM) to a calibrated reference template (red), the resulting sedimentation rate, and the match of sparse planktic $\delta^{18}O$ data (green dots) to the LR04 (black) reference template (Lisiecki and Raymo, 2005). For PC726, the Br/Al XRF ratio serves as a proxy for marine organic matter that indicates a peak at ~5 m depth that coincides with the change in $\delta^{18}O$ from 4.34 to 3.03 ‰ and back (low values up-plot) possibly corresponding to the MIS 5e.

Fig. 10. Core PC723: (a) NRM/ARM calculated using data from 20 mT (blue) and 25 mT (red) peak field AF demagnetization steps, (b) a* reflectance (black) and derivative of the color spectrum between 555 and 575 nm diagnostic of hematite (red), (c) total sum of intensities in the "organic" wavelength range (605-695 nm), (d) Ba/Al (green) and Mn/Al (orange) from XRF core scanning, (e) Br/Al (red) and Ca/Ti (light blue) from XRF core scanning with available $\delta^{18}O$ in the range from 4.43 to 3.53 ‰

plotted with low values up-plot (black dots), (f) κ_{ARM}/κ (proxy for magnetite grain size with high values indicating finer grain size), (g) sedimentation rate from trial age model based on NRM/ARM (blue) matched to the virtual dipole moment (VADM) paleointensity template (red, see text), and available $\delta^{18}O$ data (green dots) matched to the LR04 $\delta^{18}O$ template (black: Lisiecki and Raymo, 2005).

Fig. 11. ODP Site 1101: relative paleointensity proxy (NRM/ARM) from Guyodo et al. (2001) in red, matched to the RPI calibrated templates (Channell et al., 2009, 2016) in blue. The resulting sedimentation rate and volume susceptibility, on this age model, is then compared with the LR04 $\delta^{18}O$ reference template (Lisiecki and Raymo, 2005).

Table 1. Piston cores (PC) and giant box cores (GBC) recovered during Cruise JR298.

Table 2. Age-depth tie-points defining the age model for piston cores PC736, PC732, PC728 and PC726, with poorly defined age model for PC723.

References:

Acton, G., Guyodo, Y., Brachfeld, S., 2002, Magnetostratigraphy of sediment drifts on the continental rise of West Antarctica (ODP leg 178, Sites 1095, 1096, and 1101). In Barker, P.F., Camerlinghi, A. Acton G.D. Ramsey, A.T.S. (Eds.), Proceedings of the ODP, Sci. Results, 178, Ocean Drilling Program, College Station, TX.

Acton, G., Guyodo, Y., Brachfeld, S., 2006, The nature of a cryptochron from a paleomagnetic study of chron C4r.2r recorded in sediments off the Antarctic Peninsula. Phys. Earth Planet. Int., 156, 213-222.

Aragon, R., Buttrey, D.J., Shepherd, J.P., Honig, J.M., 1985. Influence of nonstoichiometry on the Verwey transition, Phys. Rev B., 31, 430–436.

Banerjee, S.K., Mellema, J.P., A new method for the determination of paleointensity from the ARM properties of rocks. Earth Planet Sci. Letters, 23, 177-184, 1974.

Barker, P.F., Osterman, L.E., Hall, M.A., 2002. Data report: Oxygen and carbon isotope measurements on *Neogloboquadrina pachyderma* (s) from Holes 1096B and 1101A, Antarctica Peninsula margin, Leg 178. In: Barker, P.F., Camerlenghi, A., Acton, G.D., Ramsay, A.T.S. (Eds.), Proc. ODP, Sci. Res., vol. 178. Texas A&M University, College Station, TX, p. 1-10 (CD-ROM).

Barker, P.F., Camerlenghi, A., Acton, G.D., et al., 1999. Proc. ODP Init. Repts., 178, 1-174 [CD-ROM]. Available from: Ocean Drilling Program, Texas A&M University, College Station, TX 77845-9547, USA.

Brachfeld, S.A., Guyodo, Y., Acton, G.D., 2001. Data Report: The magnetic mineral assemblage of hemipelagic drifts, ODP Site 1096. Barker, P.F., Camerlenghi, A., Acton, G.D., and Ramsay, A.T.S. (Eds.). Proceedings of the Ocean Drilling Program, Scientific Results, 178 1–12 [Online].

Canfield, D.E., 1989. Reactive iron in marine sediments. Geochim. Cosmochim. Acta, 53, 619-632.

Carter-Stiglitz, B., Moskowitz, B., Jackson, M.J., 2001. Unmixing magnetic assemblages and the magnetic behavior of bimodal mixtures. J. Geophys. Res., 106, 26,397-26, 411.

Channell, J.E.T., Xuan, C., 2009. Self-reversal and apparent magnetic excursions in Arctic sediments. Earth Planet. Sci. Lett., 284, 124-131.

Channell J.E.T., Hodell, D.A., 2013. Magnetic signatures of Heinrich-like detrital layers in the Quaternary of the North Atlantic, Earth Planet. Sci. Lett., 369-370, 260-270.

Channell, J.E.T., Mazaud, A., Sullivan, P., Turner, S., Raymo, M.E., 2002. Geomagnetic excursions and paleointensities in the 0.9-2.15 Ma interval of the Matuyama Chron at ODP Site 983 and 984 (Iceland Basin), J. Geophys. Res., 107 (B6), 10.1029/2001JB000491.

Channell, J.E.T., Hodell, D.A., Xuan, C., Mazaud, A., Stoner, J.S., 2008. Age calibrated relative paleointensity for the last 1.5 Myr at IODP Site U1308 (North Atlantic). Earth Planet. Sci. Lett., 274, 59-71.

Channell, J.E.T., Xuan C., Hodell, D.A., 2009. Stacking paleointensity and oxygen isotope data for the last 1.5 Myrs (PISO 1500). Earth Planet. Sci. Lett., 283, 14-23.

Channell, J.E.T., Hodell, D.A., Margari, V., Skinner, L.C., Tzedakis, P.C., Kesler, M.S., 2013. Biogenic magnetite, detrital hematite, and relative paleointensity in sediments from the Southwest Iberian Margin, Earth Planet. Sci. Lett., 376, 99-109.

Channell, J.E.T., Hodell, D.A., Curtis, J.H., 2016. Relative paleointensity (RPI) and oxygen isotope stratigraphy at IODP Site U1308: North Atlantic RPI stack for 1.2-2.2 Ma (NARPI-2200) and age of the Olduvai Subchron. Quat. Sci. Revs., 131, 1-19.

Channell, J.E.T., Hodell, D.A., Crowhurst, S.J., Skinner, L.C., Muscheler, R., 2018. Relative paleointensity (RPI) in the latest Pleistocene (10-45 ka) and implications for deglacial atmospheric radiocarbon. Quat. Sci. Revs., 191, 57-72.

Das, B., Vinebrooke, R.D., Sanchez-Azofeifa, A., Rivard, B., Wolfe, A.P., 2005. Inferring sedimentary chlorophyll concentrations with reflectance spectroscopy: a novel approach to reconstructing historical changes in the trophic status of mountain lakes. Can. J. Fish Aquat. Sci. 62, 1067–1078.

Day, R., Fuller, M., Schmidt, V.A., 1977. Hysteresis properties of titanomagnetites: grain-size and compositional dependence. Phys. Earth Planet. Int., 13, 260-267.

Deaton, B.C., Balsam, W.L., 1991. Visible spectroscopy: A rapid method for determining hematite and goethite concentration in geological materials, J. Sediment. Petrol., 61, 628–632.

De Boer, C.B, Dekkers, M.J., 1996. Grain-size dependence of rock magnetic properties for a natural maghemite. Geophysical Research letters, 23, 2815-2818.

Debret, M., Sebag, D., Desmet, M., Balsam, W., Copard, Y., Mourier, B., Susperrigui, A.-S., Arnaud, F., Bentaleb, I., Chapron, E., Lallier-Vergès, E., Winiarski, T., 2011. Spectrocolorimetric interpretation of sedimentary dynamics: The new "Q7/4 diagram". Earth Science Reviews, 109, 1-19.

Dunlop, D.J., 2002. Theory and application of the Day plot (Mrs/Ms versus Hcr/Hc) 1. Theoretical curves and tests using titanomagnetite data. J. Geophys. Res., 107, B3, 2056, doi:10.1029/2001JB000486.

Dunlop, D.J., Özdemir, O., 1997. Rock magnetism: Fundamentals and Fontiers. Cambridge University Press, 573pp.

Dunlop, D.J., Carter-Stiglitz, B., 2006. Day plots of mixtures of superparamagnetic, single domain, pseudosingle domain, and multidomain magnetites. J. Geophys. Res., 111, B12S09, doi: 10.1029/2006JB004499.

Freer, R., O'Reilly, W., 1980. The diffusion of Fe^{2+} ions in spinels with relevance to the process of maghemitization, Min. Mag., 43, 889–899.

Froelich, P.N., Klinkhammer, G.P., Bender, M.L., Luedtke, N.A., Heath, G.R., Cullen, D., Dauphin, P., Hammond, D., Hartman, B., Maynard, V., 1979. Early oxidation of organic matter in pelagic sediments of the eastern equatorial Atlantic: Suboxic diagenesis. Geochim. Cosmochim. Acta 43, 1075–1090.

Gehring, A.U., Fischer, H., Louvel, M., Kunze, K., Weidler, P.G., 2009. High temperature stability of natural maghemite: a magnetic and spectroscopic study. Geophys. J. Int., 179, 1361–1371.

Gendler, T.S., Shcherbakov, V.P., Dekkers, M.J., Gapeev, A.K., Gribov, S.K. McClelland, M., 2005. The lepidocrocite-maghemite reaction chain—I. Aquisition of chemical remanent magnetization by maghemite, its magnetic properties and thermal stability, Geophys. J. Int., 160, 815–832.

Giorgetti, A., Crise, A., Laterza, R., Perini, L., Rebesco, M., Camerlenghi, A., 2003. Water masses and bottom boundary layer dynamics above a sediment drift of the Antarctic Peninsula Pacific Margin. Antarctic Science, 15 (4), 537-546.

Guyodo, Y., Acton, G.D., Brachfeld, S., Channell, J.E.T., 2001, A sedimentary paleomagnetic record of the Matuyama Chron from the western Antarctic margin (ODP Site 1101). Earth Planet. Sci. Letters, 191, 61-74.

Guyodo, Y., Channell J.E.T., Thomas, R., 2002. Deconvolution of u-channel paleomagnetic data near geomagnetic reversals and short events. Geophys. Res. Letters, 29, 1845, doi:10.1029/2002GL014963.

Hernández-Molina, F.J., Larter, R.D., Maldonado, A. 2017. Neogene to Quaternary stratigraphic evolution of the Antarctic Peninsula, Pacific Margin offshore of Adelaide Island: Transitions from a non-glacial, through glacially-influenced to a fully glacial state. Global and Planetary Change, 156, 80–111.

Heslop, D., Dekkers, M.J., Kruiver, P.P., van Oorschot, I.H.M., 2002. Analysis of isothermal remanent magnetization acquisition curves using the expectation maximization algorithm. Geophys. J. Int. 148, 58-64.

Hillenbrand, C.-D., Grobe, H., Diekmann, B., Kuhn, G., Fütterer, D.K., 2003. Distribution of clay minerals and proxies for productivity in surface sediments of the Bellingshausen and Amundsen seas (West Antarctica) - Relation to modern environmental conditions. Mar. Geol. 193, 253-271.

Hillenbrand C.-D., Camerlenghi, A., Cowan, E.A., Hernández-Molina, F.J., Lucchi, R.G., Rebesco, M., Uenzelmann-Neben, G., 2008a. The present and past bottom-current flow regime around the sediment drifts on the continental rise west of the Antarctic Peninsula. Marine Geology, 255, 55-63.

Hillenbrand, C.-D., Moreton, S.G., Caburlotto, A., Pudsey, C.J., Lucchi, R.G., Smellie, J.L., Benetti, S., Grobe, H., Hunt, J.B., Larter, R.D., 2008b. Volcanic time-markers for Marine Isotopic Stages 6 and 5 in Southern Ocean sediments and Antarctic ice cores: implications for tephra correlations between palaeoclimatic records. Quat. Sci. Revs., 27, 518-540.

Jaccard, S.L., Galbraith, E.D., Martínez-García, A., Anderson, R.F., 2016. Covariation of deep Southern Ocean oxygenation and atmospheric CO_2 through the last ice age. Nature, 530, 207-210.

Kawamura, N., Ishikawa N., Torii, M., 2012. Diagenetic alteration of magnetic minerals in Labrador Sea sediments (IODP Sites U1305, U1306, and U1307). Geochem., Geophys, Geosystems, 13 (8), Q08013, doi:10.1029/2012GC004213.

King, J.W., Banerjee, S.K., Marvin, J., 1983. A new rock-magnetic approach to selecting sediments for geomagnetic paleointensity studies: application to paleointensity for the last 4000 years. J. Geophys. Res. 88, 5911-5921.

Kirschvink, J.L., 1980. The least squares lines and plane analysis of paleomagnetic data. Geophys. J.R. Astr. Soc. 62, 699-718.

Levi, S., Banerjee, S.K., 1976. On the possibility of obtaining relative paleointensities from lake sediments. Earth Planet. Sci. Letters, 29, 219-226.

Lisiecki, L.E., Raymo, M.E., 2005. A Pliocene-Pleistocene stack of 57 globally distributed benthic $\delta^{18}O$ records. Paleoceanography, 20, PA1003, doi:10.1029/2004PA001071.

Lowrie, W., 1990. Identification of ferromagnetic minerals in a rock by coercivity and unblocking temperature properties. Geophys. Res. Letters, 17, 159-162.

Lu, Z., Hoogakker, B.A.A., Hillenbrand, C.-D., Zhou, S., Thomas, E., Gutchess, K.M., Lu, W., Jones, L., and Rickaby, R.E.M., 2016. Oxygen depletion recorded in upper waters of the glacial Southern Ocean, Nat. Comm., 7, 11146.

Macri, P., Sagnotti, L., Lucchi, R.G., Rebesco, M., 2006. A stacked record of relative geomagnetic paleointensity for the past 270 kyr from the western continental rise of the Antarctic Peninsula. Earth. Planet. Sci. Lett., 252, 162-179.

Mangini, A., Eisenhauer, A., Walter, P., 1990. Response of manganese in the ocean to the climatic cycles in the Quaternary, Paleoceanography, 5(5), 811–821, doi:10.1029/PA005i005p00811.

Mangini, A., Jung, M., Laukenmann, S., 2001. What do we learn from peaks of uranium and of manganese in deep sea sediments?, Mar. Geol., 177, 63–78.

Oda, H., Xuan, C., 2014. Deconvolution of continuous paleomagnetic data from pass through magnetometer: A new algorithm to restore geomagnetic and environmental information based on realistic optimization, Geochem., Geophys. Geosyst., 15, 3907-3924, doi:10.1002/2014GC005513.

Özdemir, O., Banerjee, S.K., 1984. High temperature stability of maghemite (γ-Fe_2O_3), Geophys. Res. Lett., 11(3), 161–164, doi:10.1029/GL011i003p00161.

Özdemir, O ., D. J. Dunlop, and B. M. Moskowitz, 1993. The effect of oxidation on the Verwey transition in magnetite, Geophys. Res. Lett., 20, 1671 – 1674, doi:10.1029/93GL01483.

Petersen, N., Vali, H., 1987. Observation of shrinkage cracks in ocean floor titanomagnetites. Phys. Earth. Planet. Int., 46, 197-205.

Rebesco, M., Larter, R. D., Camerlenghi, A., Barker, P. F., 1996. Giant sediment drifts on the continental rise west of the Antarctic Peninsula. Geo-Marine Letters, 16, 65–75.

Rebesco, M., Pudsey, C., Canals, M., Camerlenghi, A., Barker, P., Estrada, F., Giorgetti, A. 2002. Sediment drift and deep-sea channel systems, Antarctic Peninsula Pacific Margin. In: Stow, D.A.V., Pudsey, C.J., Howe, J.A., Faugeres, J.C., Viana, A.R. (Eds.), Deep-Water Contourite Systems: Modern Drifts and Ancient Series. Seismic and Sedimentary Characteristics. Geol. Soc. London Memoir, 22, 353–371.

Reilly, B. T., Natter, C.J., Brachfeld, S.A., 2016. Holocene glacial activity in Barilari Bay, west Antarctic Peninsula, tracked by magnetic mineral assemblages: Linking ice, ocean, and atmosphere, Geochem. Geophys. Geosyst., 17, 4553–4565, doi:10.1002/2016GC006627.

Sagnotti, L., Macri, P., Camerlenghi, A., Rebesco, M., 2001. Environmental magnetism of Antarctic late Pleistocene sediments and interhemispheric correlation of climatic events. Earth Planet. Sci. Lett. 192, 65-80.

Shipboard Scientific Party, 1999. Site 1101. In: Barker, P.F., Camerlenghi, A., Acton, G.D. (eds.) Proc. ODP, Init. Repts, 178, 1-83, Available from Ocean Drilling Program, Texas A&M University, College Station TX 77845-9547.

Smirnov A.V., Tarduno, J.A., 2000. Low-temperature magnetic properties of pelagic sediments (Ocean Drilling Program Site 805C): Tracers of maghemitization and magnetic mineral reduction. J. Geophys. Res., 105 (B7), 16457-16471.

Stein, R., Schubert, C.J., MacDonald, R.W., Fohl, K., Harvey, H.R., Weiel, D., 2003. The central Arctic Ocean: distribution, sources, variability, and burial of organic carbon. In: Stein, R., MacDonald, R.W. (Eds.), The organic carbon cycle in the Arctic

Ocean. Springer-Verlag, Berlin, pp. 295–314.

Tauxe, L., 1993. Sedimentary records of relative paleointensity of the geomagnetic field: theory and practice. Rev. Geophys., 31, 319-354.

Thomas, R., Guyodo Y., Channell, J.E.T., 2003, U-channel track for susceptibility measurements. Geochemistry, Geophysics and Geosystems (G^3), 1050, doi: 10.1029/2002GC000454.

Torii, M., 1997. Low-temperature oxidation and subsequent downcore dissolution of magnetite in deep-sea sediments, ODP Leg 161 (Western Mediterranean). J. Geomag. Geoelectr., 49, 1233-1245.

Vautravers, M., Hodell, D.A., Channell, J.E.T., Hillenbrand, C.-D., Hall, M., Smith J., Larter, R.D., 2013. Palaeoenvironmental records from the West Antarctic Peninsula drift sediments over the last 75 ka. In: Hambrey, M.J, Barker, P.F., Barrett, P.J., Bowman, V., Davies, B., Smellie, J.L. and Tranter, M. (eds.), Antarctic Palaeoenvironments and Earth-Surface processes. Geological Society, London, Special Publications, 381, http://dx.doi.org/10.1144/SP381.12.

Venuti, A., Florindo, F., Carburlotto, A., Hounslow, M.W., Hillenbrand, C.-D., Strada, E., Talarico F.M., Cavallo, A., 2011. Late Quaternary sediments from deep-sea sediment drifts on the Antarctic Peninsula Pacific margin: Climatic control on provenance of minerals. J. Geophys. Res., 116, B06104, doi:10.1029/2010JB007952.

Weeks, R., Laj, C., Endignoux, L., Mazaud, A., Labeyrie, L., Roberts, A.P., Kissel, C., Blanchard, E., 1995. Normalized NRM intensity during the last 240,000 years in piston cores from the central North Atlantic Ocean: geomagnetic field intensity or environmental signal? Phys. Earth Planet. Inter., 87, 213-229.

Westrich, J.T., Berner, R.A., 1984. The role of sedimentary organic matter in bacterial sulfate reduction: The G model tested. Limnol. Oceanogr. 29 (2), 236–249.

Xuan, C., Channell, J.E.T., 2009. UPmag: MATLAB software for viewing and processing u-channel or other pass-through paleomagnetic data. Geochem. Geophys. Geosyst., 10, Q10Y07, doi:1029/2009GC002584.

Xuan, C., Channell, J.E.T., 2010. Origin of apparent magnetic excursions in deep-sea sediments from Mendeleev-Alpha Ridge, Arctic Ocean, Geochem. Geophys. Geosyst., 11, Q02003, doi:10.1029/2009GC002879.

Xuan, C., Channell, J.E.T., Polyak, L., Darby, D.A., 2012. Paleomagnetism of Quaternary sediments from Lomonosov Ridge and Yermak Plateau: Implications for age models in the Arctic Ocean. Quaternary Science Reviews, 32, 48-63.

Yamazaki, T., Solheid, P., 2011. Maghemite-to-magnetite reduction across the Fe-redox boundary in a sediment core from the Ontong-Java Plateau: influence on relative paleointensity estimation and environmental magnetic application. Geophys. J. Int., 185, 1243-1254.

Ziegler, M., Jilbert, T., de Lange, G.J., Lourens, L.J., Reichart, G.-J., 2008. Bromine counts from XRF scanning as an estimate of the marine organic carbon content of sediment cores. Geochem. Geophys. Geosyst., 9 , Q05009, doi:10.1029/2007GC001932.

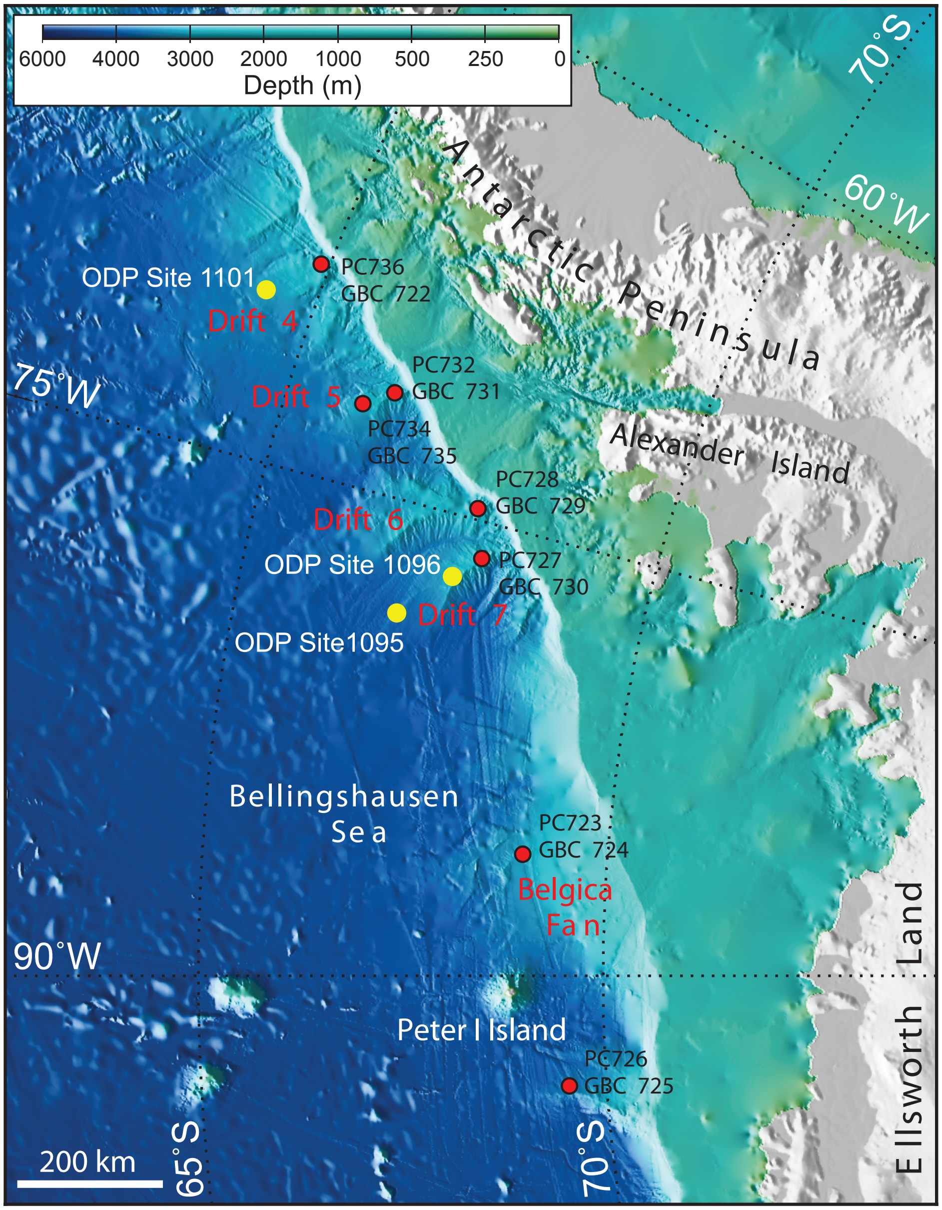

6000 4000 3000 2000 1000 500 250 0
Depth (m)
70°S
60°W
Antarctic Peninsula
Alexander Island
ODP Site 1101
PC736
GBC 722
Drift 4
75°W
PC732
GBC 731
Drift 5
PC734
GBC 735
PC728
GBC 729
Drift 6
ODP Site 1096
PC727
GBC 730
Drift 7
ODP Site1095
Bellingshausen
Sea
PC723
GBC 724
Belgica
Fan
90°W
Peter I Island
PC726
GBC 725
Ellsworth Land
200 km
65°S
70°S

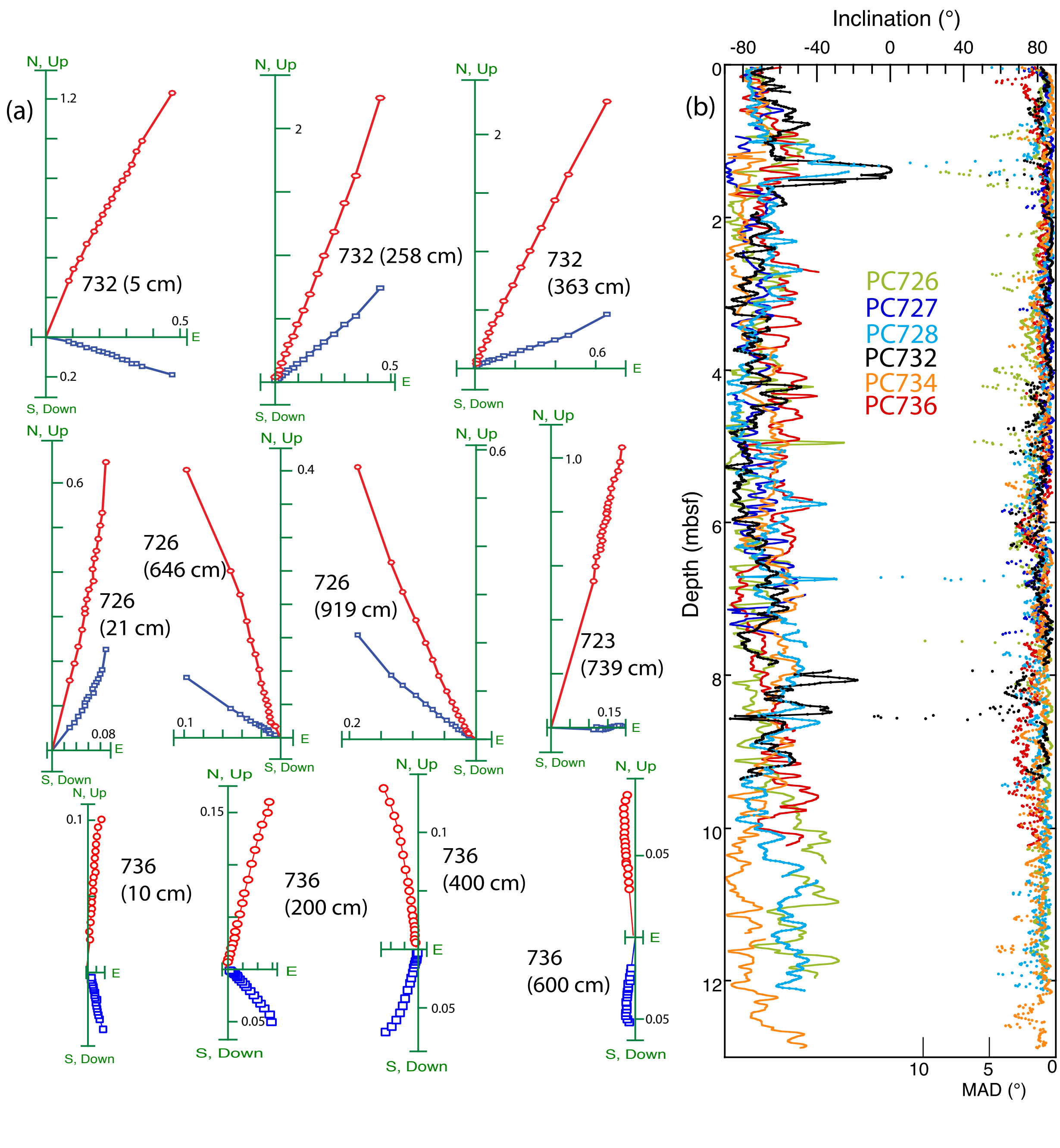

(a)
732 (5 cm)
732 (258 cm)
732
(363 cm)
726
(646 cm)
726
(21 cm)
726
(919 cm)
723
(739 cm)
736
(10 cm)
736
(200 cm)
736
(400 cm)
736
(600 cm)
N, Up
S, Down
E
(b)
Inclination (°)
Depth (mbsf)
MAD (°)
PC726
PC727
PC728
PC732
PC734
PC736

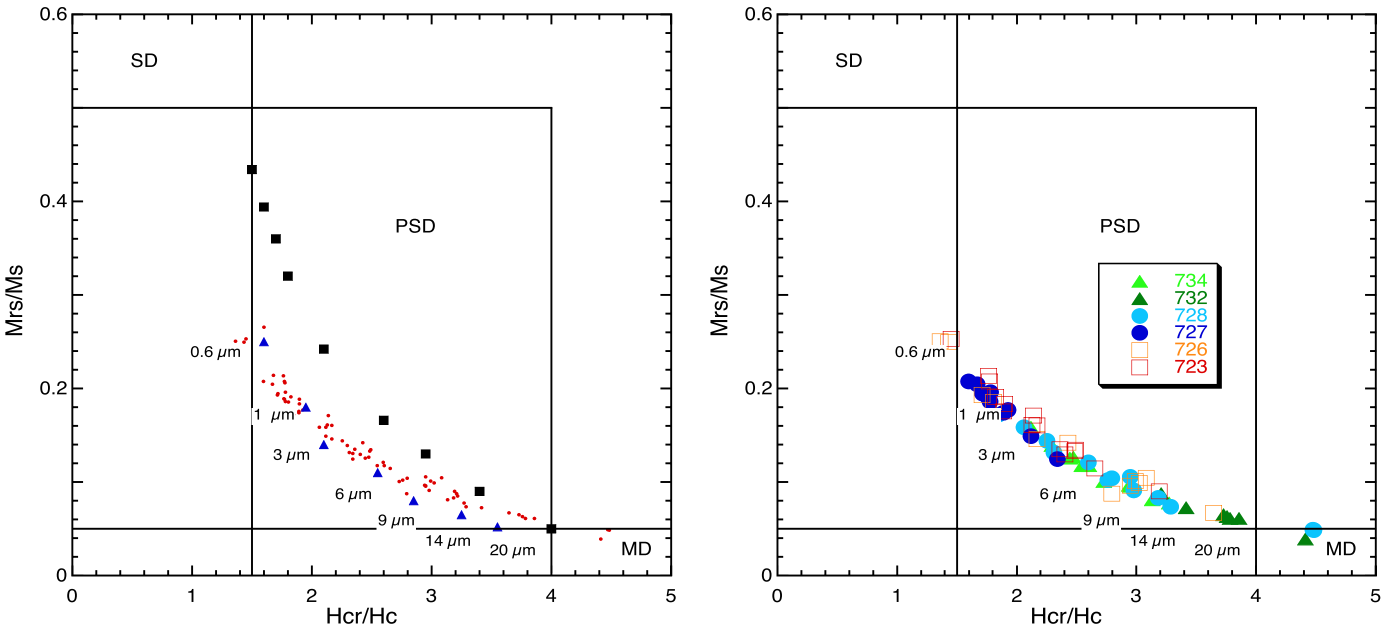

0.6
0.4
0.2
0
Mrs/Ms
SD
PSD
MD
0.6 μm
1 μm
3 μm
6 μm
9 μm
14 μm
20 μm
0
1
2
3
4
5
Hcr/Hc
0.6
0.4
0.2
0
Mrs/Ms
SD
PSD
MD
0.6 μm
1 μm
3 μm
6 μm
9 μm
14 μm
20 μm
734
732
728
727
726
723
0
1
2
3
4
5
Hcr/Hc

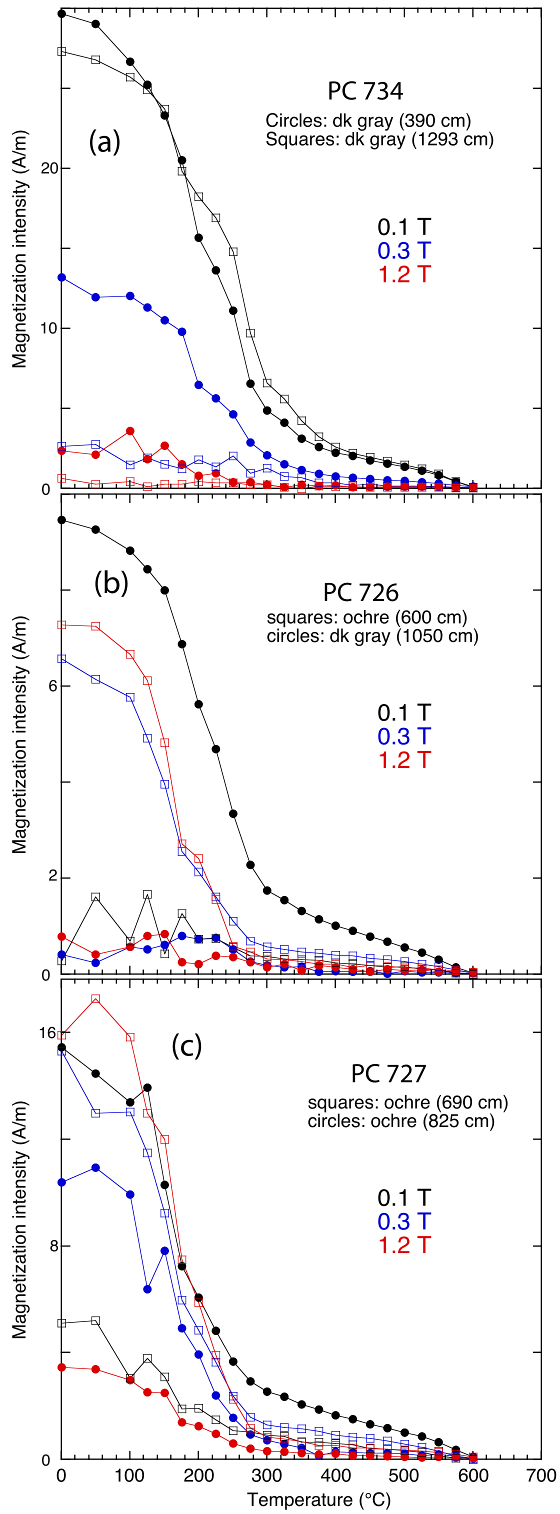

PC 734
Circles: dk gray (390 cm)
Squares: dk gray (1293 cm)
(a)
0.1 T
0.3 T
1.2 T
(b)
PC 726
squares: ochre (600 cm)
circles: dk gray (1050 cm)
0.1 T
0.3 T
1.2 T
(c)
PC 727
squares: ochre (690 cm)
circles: ochre (825 cm)
0.1 T
0.3 T
1.2 T
Magnetization intensity (A/m)
Temperature (°C)
0
100
200
300
400
500
600
700

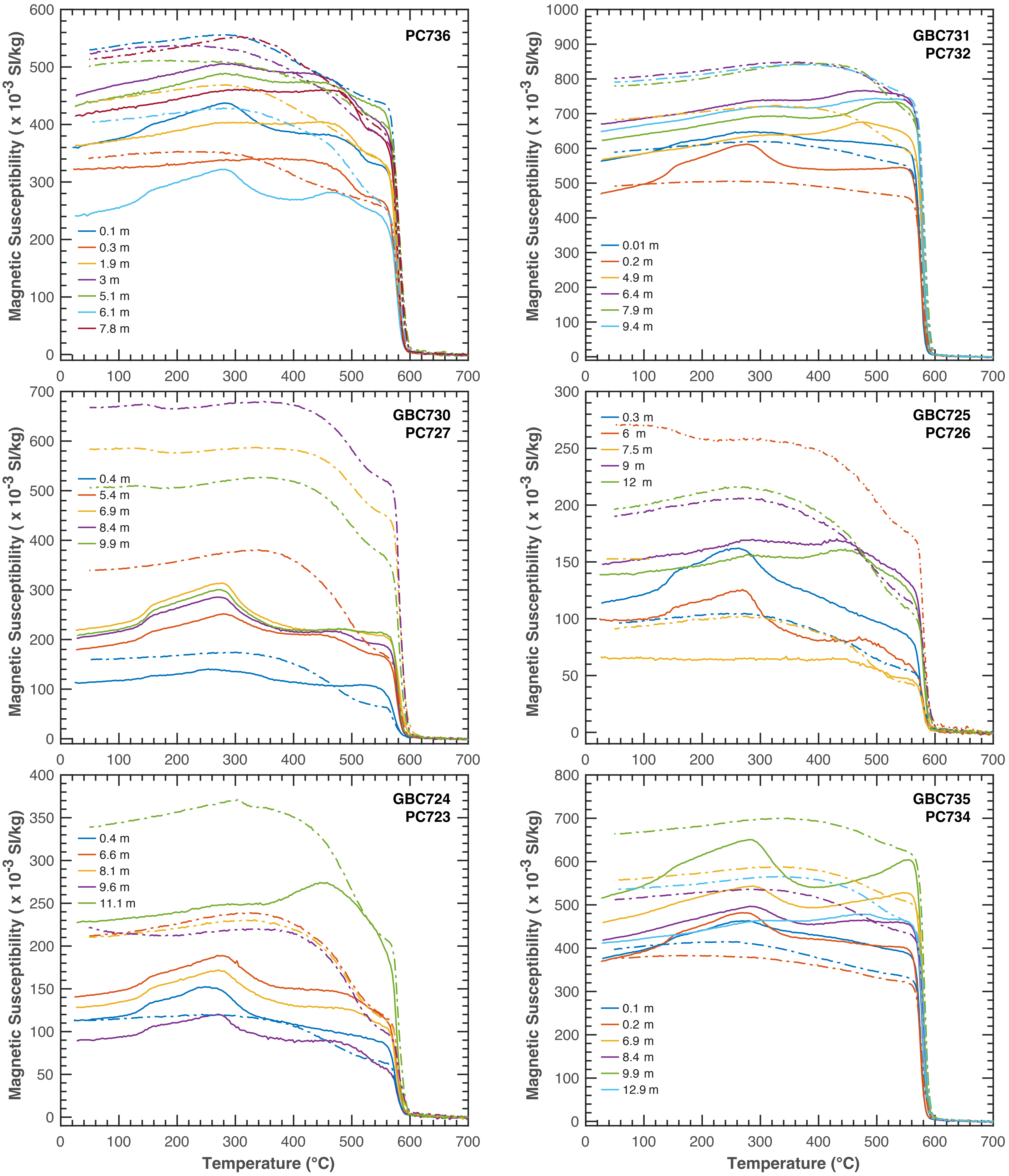

PC736
0.1 m
0.3 m
1.9 m
3 m
5.1 m
6.1 m
7.8 m
GBC731
PC732
0.01 m
0.2 m
4.9 m
6.4 m
7.9 m
9.4 m
GBC730
PC727
0.4 m
5.4 m
6.9 m
8.4 m
9.9 m
GBC725
PC726
0.3 m
6 m
7.5 m
9 m
12 m
GBC724
PC723
0.4 m
6.6 m
8.1 m
9.6 m
11.1 m
GBC735
PC734
0.1 m
0.2 m
6.9 m
8.4 m
9.9 m
12.9 m
Magnetic Susceptibility (x 10-3 SI/kg)
Temperature (°C)

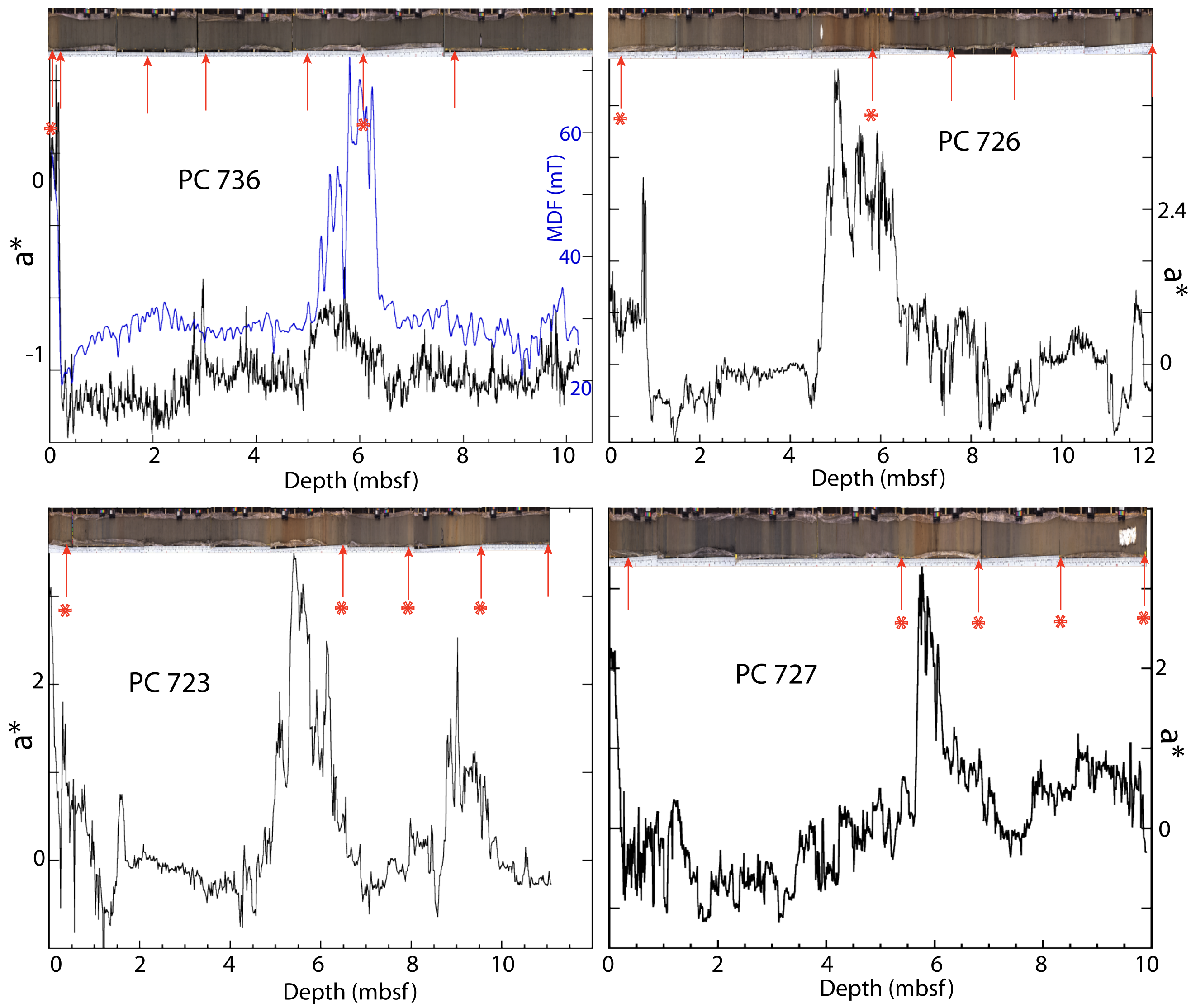

PC 736
PC 726
PC 723
PC 727
a*
MDF (mT)
Depth (mbsf)

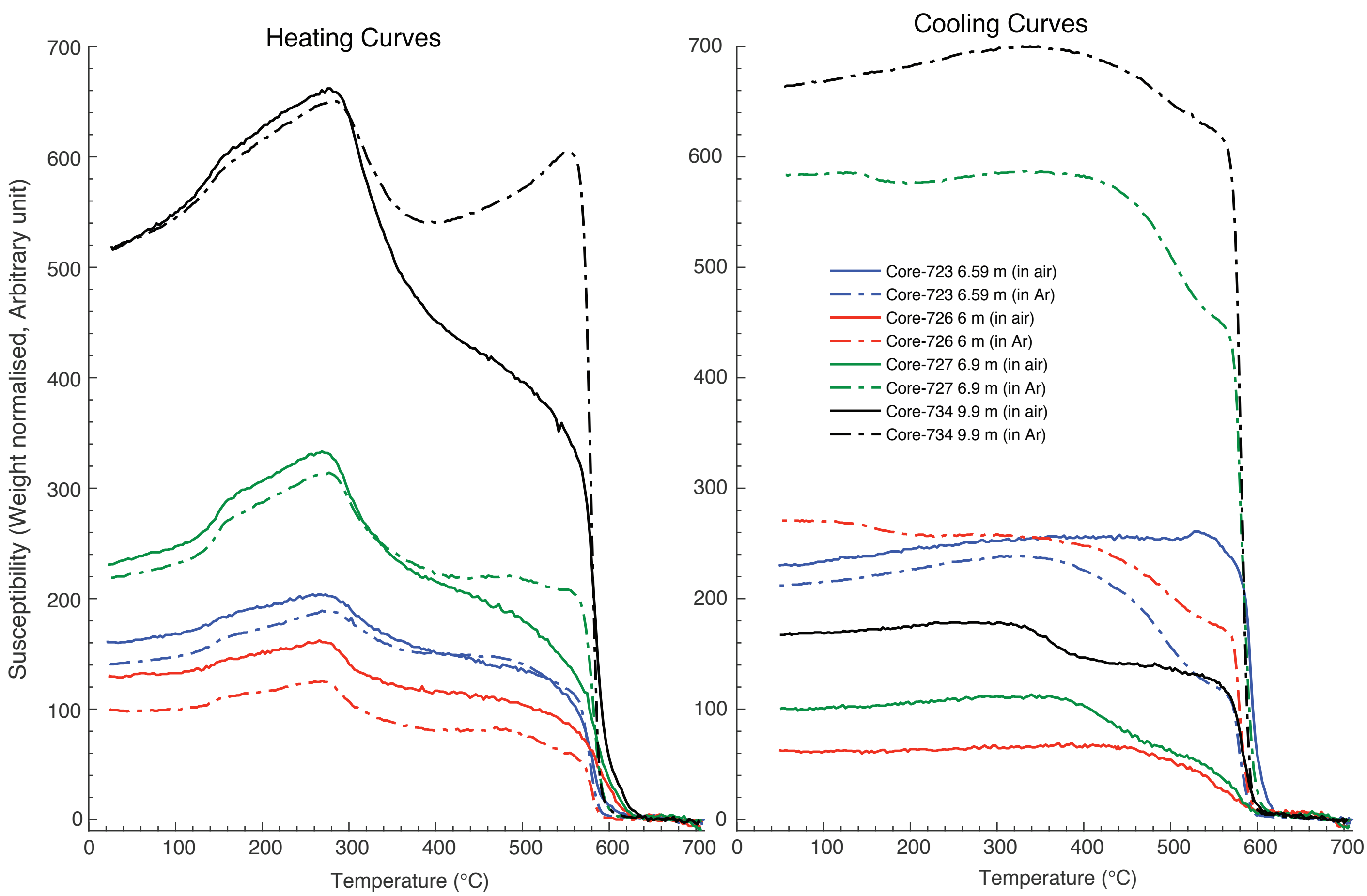
Heating Curves
Cooling Curves
Susceptibility (Weight normalised, Arbitrary unit)
Temperature (°C)
Temperature (°C)
Core-723 6.59 m (in air)
Core-723 6.59 m (in Ar)
Core-726 6 m (in air)
Core-726 6 m (in Ar)
Core-727 6.9 m (in air)
Core-727 6.9 m (in Ar)
Core-734 9.9 m (in air)
Core-734 9.9 m (in Ar)

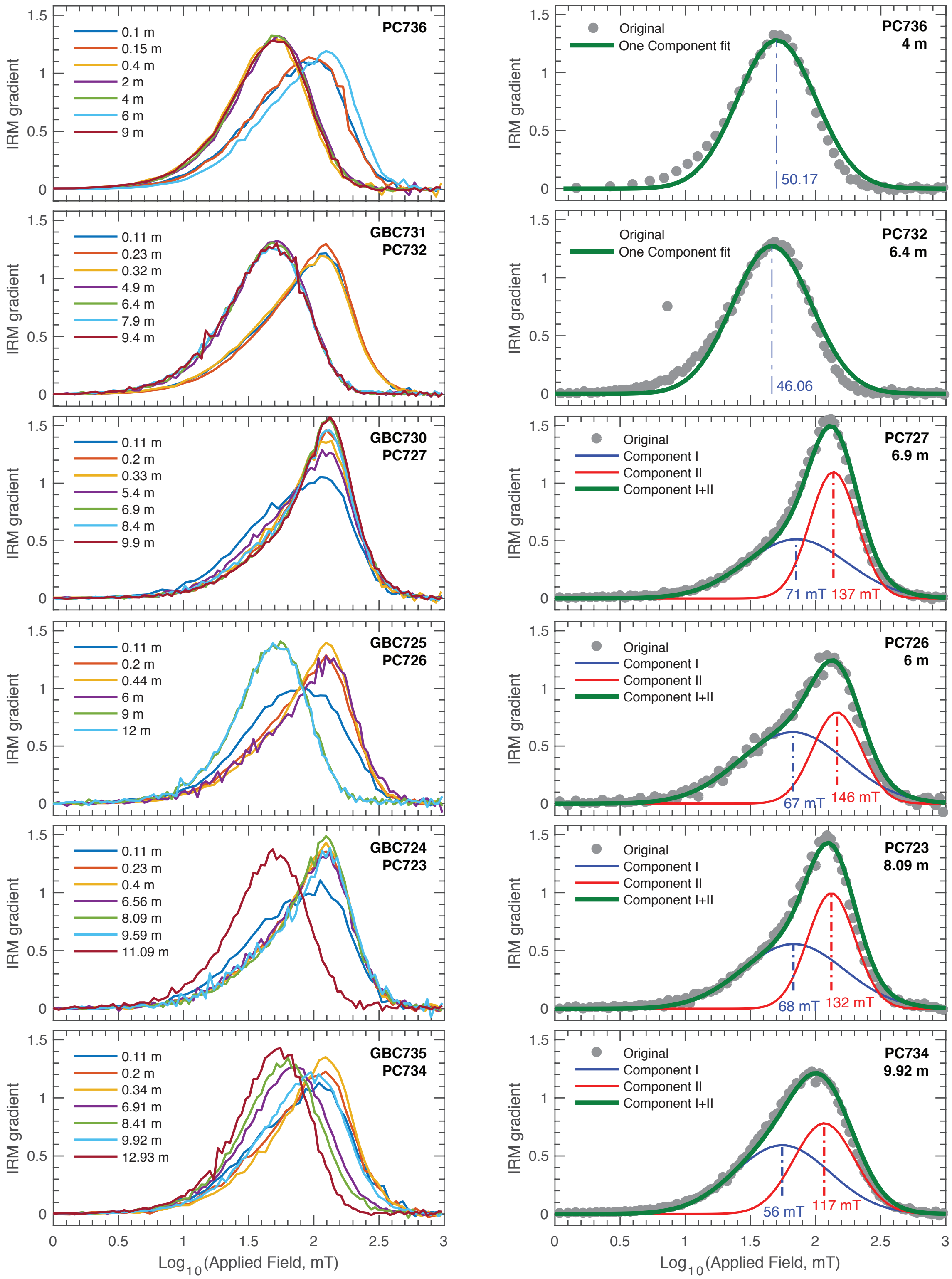

PC736
0.1 m
0.15 m
0.4 m
2 m
4 m
6 m
9 m
GBC731
PC732
0.11 m
0.23 m
0.32 m
4.9 m
6.4 m
7.9 m
9.4 m
GBC730
PC727
0.11 m
0.2 m
0.33 m
5.4 m
6.9 m
8.4 m
9.9 m
GBC725
PC726
0.11 m
0.2 m
0.44 m
6 m
9 m
12 m
GBC724
PC723
0.11 m
0.23 m
0.4 m
6.56 m
8.09 m
9.59 m
11.09 m
GBC735
PC734
0.11 m
0.2 m
0.34 m
6.91 m
8.41 m
9.92 m
12.93 m
IRM gradient
Log10(Applied Field, mT)
Original
One Component fit
PC736
4 m
50.17
PC732
6.4 m
46.06
Component I
Component II
Component I+II
PC727
6.9 m
71 mT
137 mT
PC726
6 m
67 mT
146 mT
PC723
8.09 m
68 mT
132 mT
PC734
9.92 m
56 mT
117 mT

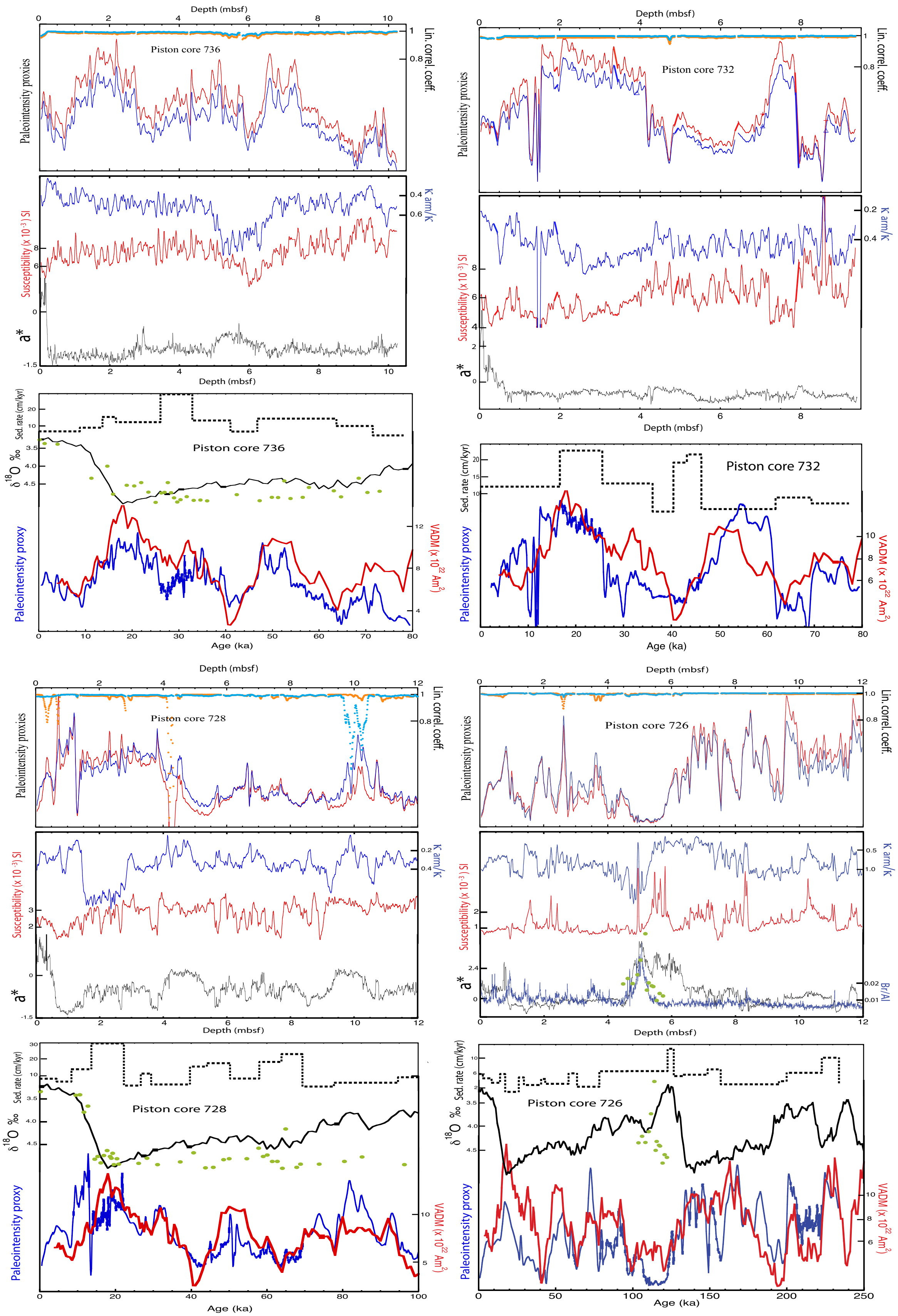
Depth (mbsf)
Piston core 736
Lin. correl. coeff.
Paleointensity proxies
Susceptibility (x 10^{-3}) SI
K arm/K
a*
Sed. rate (cm/kyr)
$\delta^{18}O$ ‰
Paleointensity proxy
VADM (x 10^{22} Am^2)
Age (ka)
Piston core 732
Piston core 728
Piston core 726
Br/Al

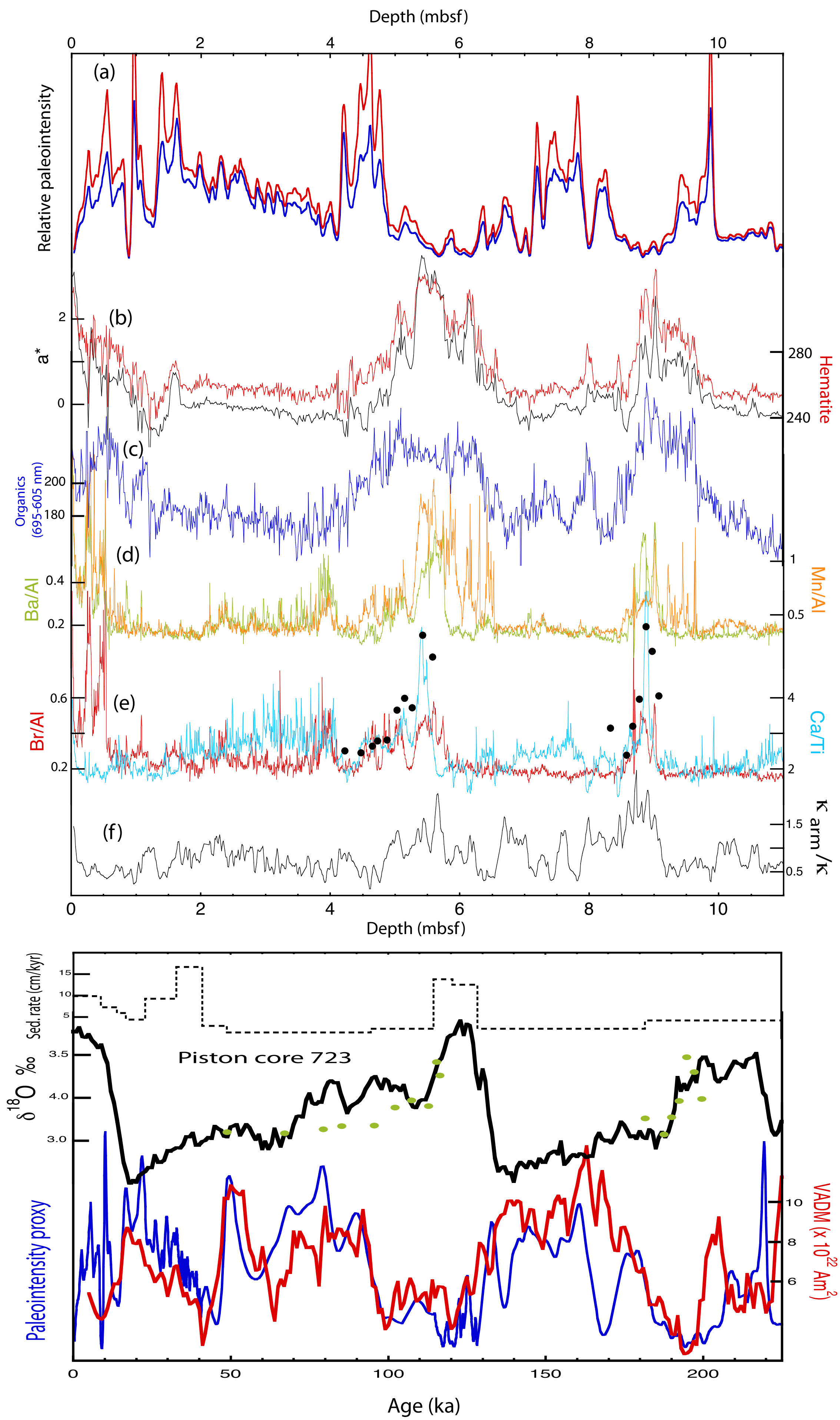

Depth (mbsf)
(a)
Relative paleointensity
(b)
a*
Hematite
(c)
Organics (695-605 nm)
(d)
Ba/Al
Mn/Al
(e)
Br/Al
Ca/Ti
(f)
κarm/κ
Depth (mbsf)
Sed. rate (cm/kyr)
Piston core 723
δ18O ‰
Paleointensity proxy
VADM (x 10^22 Am^2)
Age (ka)

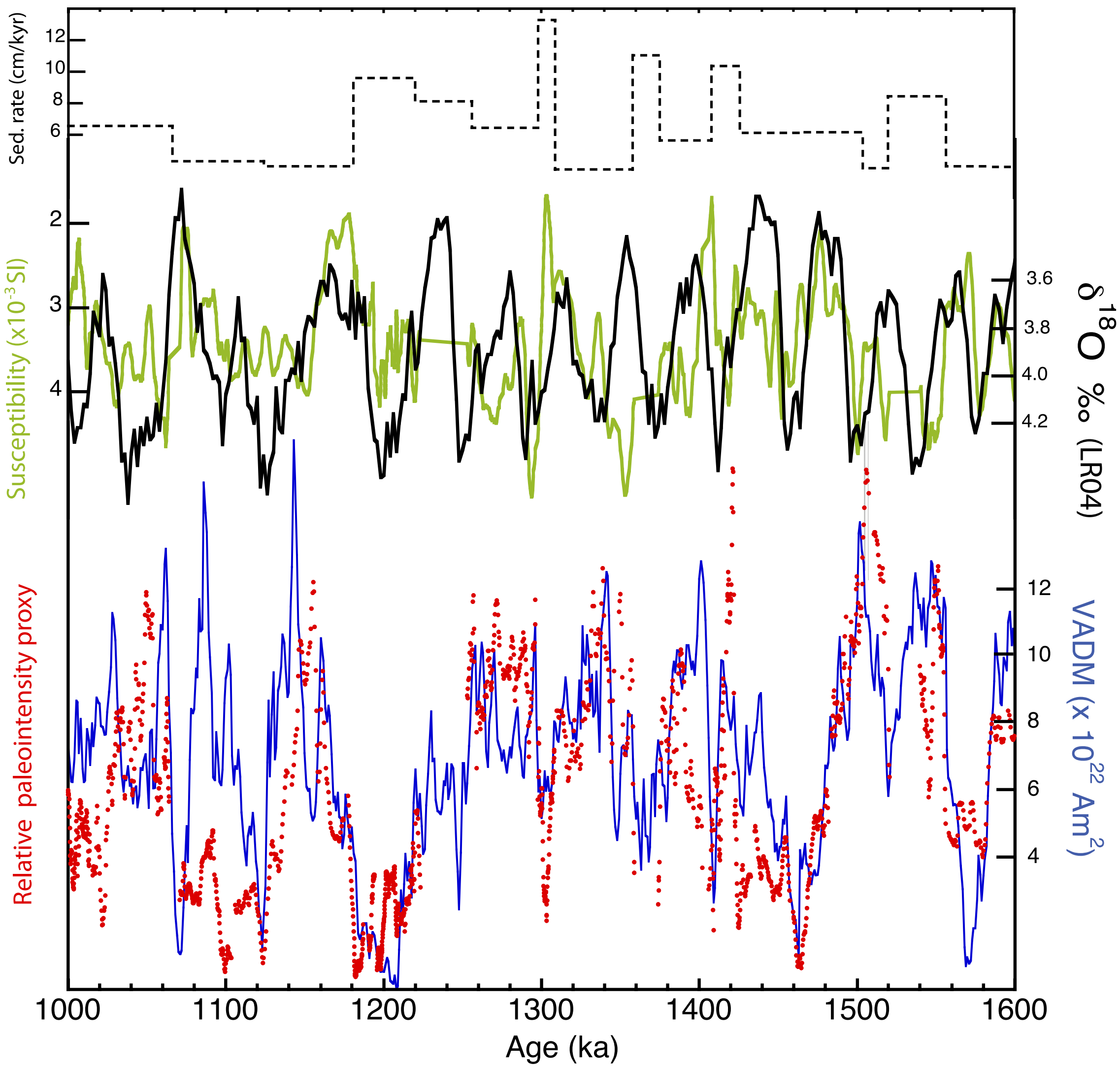

Sed. rate (cm/kyr)
12
10
8
6
2
3
4
Susceptibility (x10^{-3} SI)
3.6
3.8
4.0
4.2
δ^{18}O ‰ (LR04)
Relative paleointensity proxy
12
10
8
6
4
VADM (x 10^{22} Am^2)
1000
1100
1200
1300
1400
1500
1600
Age (ka)

Table 1. Piston and giant box cores collected during JR 298

Piston Core (PC)	Giant Box Core (GBC)	Location (IODP label)	Latitude (°S)	Longitude (°W)	Water Depth (m)	PC length (m)
723	724	Site BELS-1	68° 56.57'	85° 47.42'	3075	11.09
726	725	Site BELS-2C	69° 31.90'	93° 54.95'	3663	12.00
727	730	Near crest of Drift 7 Site PEN-4B	67° 51.86'	76° 10.76'	2681	9.90
728	729	Crest of Drift 6, Site PEN-3B	67° 40.10'	74° 38.54'	2454	12.17
732	731	Crest of Drift 5, Site PEN-2B	66° 16.33'	71° 54.51'	2647	9.40
734	735	Crest of Drift 5	65° 56.29'	72° 31.05'	3000	12.93
736	722	Crest of Drift 4, Site PEN-1	64° 53.72'	69° 02.13'	2325	10.26

Table 2. Depth-age tie-points for piston cores 736, 732, 728, 726 and 723.

736 (m)	736 (ka)	732 (m)	732 (ka)	728 (m)	728 (ka)	726 (m)	726 (ka)	723 (m)	723 (ka)
0.00	0.00	0.00	0.00	0.00	0.00	0.00	0.0000	0.00	0.0000
0.66	8.75	2.08	16.66	0.35	4.44	0.17	2.7700	0.87	8.8000
1.13	13.60	4.14	25.57	0.58	8.33	0.43	8.3300	1.23	13.800
1.60	16.52	5.55	36.11	1.32	13.61	0.63	13.880	1.40	16.660
2.83	26.00	5.78	40.50	3.97	22.22	0.83	17.220	1.67	22.770
4.86	32.86	6.33	43.33	4.12	26.66	0.93	26.100	2.60	32.770
6.00	41.00	7.00	46.38	4.43	29.44	1.10	29.400	3.97	41.000
6.43	46.78	7.92	61.94	4.86	39.72	1.43	40.500	4.20	48.880
9.00	63.77	8.61	69.44	5.56	44.16	1.56	43.300	4.83	94.740
9.83	71.55	9.19	77.22	6.65	50.27	2.06	58.300	5.28	114.50
10.16	78.00			7.27	58.05	2.40	63.800	6.11	120.50
				8.36	63.88	2.77	78.330	7.10	128.38
				9.68	69.44	3.97	96.110	8.30	181.66
				9.91	77.78	5.77	122.77	8.86	195.00
				10.81	94.72	6.27	126.66		
				11.20	99.16	6.57	132.20		
						7.53	148.88		
						8.13	157.22		
						9.33	195.00		
						9.53	200.00		
						9.97	206.94		
						11.63	222.91		
						11.96	234.00		